Hydrodynamic instabilities in shallow reservoirs

Travail de fin d'études réalisé en vue de l'obtention du grade de Master Ingénieur Civil des Constructions par DE CUYPER Anaïs

Composition du jury :

DEWALS Benjamin (Promoteur)
ERPICUM Sébastien (Co-promoteur)
PIROTTON Michel
ANDRIANNE Thomas
MOUZELARD Thibaut (Membre Extérieur)

Acknowledgements

Enoncé : Instabilités hydrodynamiques dans des réservoirs peu profonds

Les réservoirs peu profonds sont couramment utilisés en hydraulique urbaine et fluviale. On trouve deux grands types de réservoirs : les bassins de rétention destinés au stockage de grandes quantités d'eau et les bassins de dépollution. Dans le premier type de réservoirs, on cherche à minimiser les dépôts, contrairement au deuxième où l'objectif consiste à intercepter un maximum de sédiments. Afin de dimensionner correctement ces réservoirs en fonction de leur rôle spécifique, les capacités actuelles de prédiction des écoulements se développant dans ces réservoirs doivent être améliorées.

Ce travail comporte deux parties : une contribution expérimentale et une étude analytique. Dans la première partie, trois séries de tests seront réalisées sur un modèle réduit au laboratoire du HECE. La première permettra à l'étudiante de valider son protocole expérimental en comparant les résultats qu'elle obtient avec ceux de Peltier et al. (2014a,b, 2015). Les deux séries suivantes seront originales et permettront la caractérisation d'écoulements oscillants dans des configurations géométriques inédites. Celles-ci viseront en particulier à déterminer l'influence des caractéristiques géométriques du réservoir et des éventuels effets d'échelle sur les propriétés des jets oscillants obtenus (fréquence et longueur d'onde).
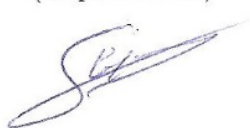
Dans la seconde partie du travail, l'étudiante explorera la mise au point d'un modèle mathématique original destiné à prédire de manière macroscopique certaines caractéristiques des écoulements sur base d'un principe de "puissance maximale". Les potentialités d'une telle approche de modélisation seront évaluées par comparaison avec des simulations numériques détaillées menées à l'aide du logiciel WOLF2D développé au sein du HECE.

Signatures des membres du jury :

Benjamin Dewals
(promoteur)

Sébastien Erpicum
(co-promoteur)

Michel Pirotton

Thomas Andrianne

Thibaut Mouzelard (Membre extérieur)

Abstract

Hydrodynamic instabilities in shallow reservoirs
DE CUYPER Anaïs
Second year of the Master's degree in Civil Engineering
Academic year 2014-2015

This Master's thesis is devoted to the study of flows in shallow reservoirs. The main purpose is to enhance the knowledge of the different flow regimes in order to improve the prediction of deposits and thus the reservoir man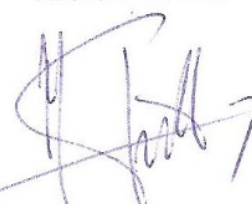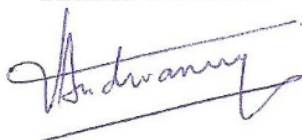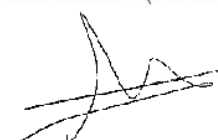agement. To do this, two points are covered in this thesis: the influence of geometric parameters (length and width of the reservoir) on main characteristics of meandering flows and the applicability of thermodynamic principles to predict the flow regime in reservoirs. Concerning the first point, three experiments were performed in a shallow horizontal flume, the first experiment being used to validate the experimental protocol. For each experiment, the surface velocity fields were measured by Large-Scale Particle Image Velocimetry (LSPIV) and the main characteristics of measured meandering flows such as the characteristic lengths or the Strouhal number were obtained using a Proper Orthogonal Decomposition (POD). Finally, it was shown that for a given flow regime, the characteristics of the flow do not depend on the geometry but only on the shallowness of the reservoir. In the second part, two analytical models were developed to model symmetric and asymmetric flows. Mass and momentum balance equations were established and the power developed by the shear force was determined for each model and compared. Based on this comparison, it was shown that the principle of maximum power could be used to determine the flow regime in reservoirs.

Résumé

Instabilités hydrodynamiques dans les réservoirs peu profonds
DE CUYPER Anaïs
Deuxième année du grade de master en ingénieur civil des constructions (finalité approfondie)
Année académique 2014-2015

Ce travail de fin d'études est consacré à l'étude des écoulement en réservoirs peu profonds. L'objectif principal est d'étendre les connaissances des différents régimes d'écoulement afin d'améliorer la prédiction des dépôts et donc, la gestion des réservoirs. Pour ce faire, deux points sont couverts dans cette thèse: l'influence des paramètres géométriques (longueur et largeur du réservoir) sur les caractéristiques principales des écoulements oscillants et l'applicabilité de principes thermodynamiques pour prédire le régime d'écoulement dans les réservoirs. Concernant le premier point, trois expériences ont été réalisées dans un canal horizontal peu profond, la première expérience étant utilisée afin de valider le protocole expérimental. Pour chaque expérience, les champs de vitesses à la surface ont été mesurés par LSPIV et les caractéristiques principales des écoulements oscillants mesurés tels que les longueurs caractéristiques ou le nombre de Strouhal ont été obtenus en utilisant la POD (Decomposition orthogonale). Au final il a été montré que pour un régime d'écoulement donné, les caractéristiques de l'écoulement ne dépendent pas de la géométrie mais seulement de la faible profondeur du réservoir. Dans la seconde partie, deux modèles analytiques ont été développés pour modéliser les écoulements symétriques et asymétriques. Les équations de continuité et de quantité de mouvement ont été établies et la puissance développée par la force de cisaillement a été déterminée pour chacun des modèles et comparée. Sur base de cette comparaison, il a été montré que le principe de la puissance maximum pouvait être utilisé pour déterminer le régime d'écoulement dans les réservoirs.

Table of contents

1 General introduction

Shallow reservoirs are structures that are commonly used in hydraulic engineering. These can play two distinct roles: they can protect against flooding, these basins are called storage reservoirs or they can be used to trap pollutants or sediments, in this case, they are called settling basins. In the first type of reservoirs, it is necessary to minimize sediment deposits while for the second, they must be maximized.

Prediction of the amount and the location of sediment deposits is therefore necessary to improve reservoir management. However, this prediction depends on the knowledge of the flow behavior which is very complex for such a simple structure (Camnasio et al. (2011); Dufresne et al. (2010)).

Dufresne et al. (2010) and Peltier et al. (2014a) showed that there was four types of flows that con occur in rectangular shallow reservoirs : Symmetric, asymmetric, meandering and instable. In the literature, the symmetric and asymmetric flows have already been well treated.

This Master's thesis will be divided into two parts. In the first one, the study focuses on meandering jets and particularly, on the influence of the reservoir geometry on the main characteristics of the flow. To do this, three experiments were be performed in a flume in the Laboratory of engineering hydraulics of the University of Liège in Belgium. Methods such as Large-Scale Particle Image Velocimetry or Proper Orthogonal Decomposition will be used to extract the results that will then be analyzed.

To date, numerical models have been used to predict flow fields. However, these require time and a lot of data. Th second part of this thesis will be devoted to the development of simple analytical models which will allow to represent phenomena occurring in symmetric and asymmetric flows. The applicability of thermodynamic principles to predict the flow regime will also be discussed.

2 State of the art

2.1 Hydrodynamics and deposit patterns

Shallow reservoirs are commonly used in hydraulic engineering and can be classified into two types :

— The settling basins are used for storm-water treatment and to limit the release of unwanted sediment in irrigation systems. In order to fulfill its role, it is necessary to maximize the sedimentation in the reservoir.

— The storage reservoirs, which are used to control flooding or to generate hydro-power, are designed to minimize sediment deposits and thus keep a large volume of clear water.

As explained by Dufresne et al. (2012), an improper sizing of these storage basins can cause significant operating costs since sediments will often have to be removed while in the case of settling reservoirs, it may lead to high concentrations of suspended load in overflows, which will be damageable for the systems downstream from the reservoir.

Most design methods only determine the volume of the reservoir and do not account for the shape nor the flow fields. However, the optimal design of such structures actually requires the perfect knowledge of the flow behavior and of the sedimentation patterns. Even if shallow reservoirs are simple structures, the flows developing in it are complex, which also affect sediment transport.

Dufresne et al. (2012) showed that there are several types of flows that can develop in rectangular shallow reservoirs. His classification was completed by Peltier et al. (2014a) who also demonstrated that the flow regime depends on the Froude number F at the reservoir inlet and on the shape factor SF that was introduced by Dufresne et al. (2012). These two parameters can be written as :

$$F = \frac{U_{in}}{\sqrt{gH}} \quad \text{and} \quad SF = \frac{L}{\Delta B^{0.6} b^{0.4}} \tag{1}$$

with U_{in} the velocity at the inlet, H the mean water depth in the reservoir, L the reservoir length, b the width of the inlet and ΔB the width of the sudden expansion of the reservoir.

Based on these two parameters, the flow pattern can be:

— Symmetric, the main jet remains straight ($F < 0.21$ and $SF \leq 6.2$),
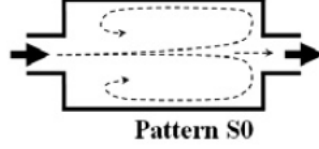
FIGURE 1 – Scheme of symmetrical flow (S0) - [Dufresne et al. (2012)]

– Asymmetric, the jet reattaches one or several times the lateral walls of the reservoir ($SF < 8.1$ whatever the Froude number is) ,
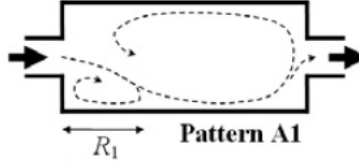
FIGURE 2 – Scheme of asymmetrical flow with only one reattachment point (A1) - [Dufresne et al. (2012)]

  – Instable, the flow does not stabilize and randomly change between symmetric and asymmetric configurations ($F \sim 0.21$ and $SF < 6.2$ or $F > 0.21$ and $6.2 < SF < 8.1$),

  – Meandering, the jet oscillates from the inlet to the outlet ($F > 0.21$ and $SF < 6.2$).

The first three types of flow pattern are now well documented in literature. Concerning the meandering flows, Camnasio et al. (2014) studied the influence of the shape factor SF on the mean kinetic energy content of the reservoir and showed that there is a linear relationship between the normalized mean kinetic energy and the logarithm of the shape factor SF.

Peltier et al. (2014c) analyzed the impact of the shallowness on coherent structures using the classification of friction regimes defined by Chu et al. (2004) and considering two regimes : frictional and non-frictional, the transition between the two taking place for a friction number S of 0.07 which is defined as:

$$S = C_f \frac{\Delta B}{8H} \qquad (2)$$

with C_f the friction coefficient.

Peltier et al. (2014c) demonstrated that the shallowness have an impact on the position where the small structures merged into large structures.

2.2 Thermodynamic principles

As hydraulic systems become more complex, thermodynamic principles enables to estimate model parameters and to characterize water behavior. These principles are based on the fact that « *nature organizes itself in such a way that its functioning is optimal under given external forcing during steady state conditions* » [Westhoff and Zehe (2013)].

To date, these principles were applied to different systems. Thus, for example, in 1979, Paltridge (1979) used thermodynamic principles to evaluate the atmospheric heat flux from the equator to the poles or more recently, Schymanski et al. (2009) used them to determine the optimized net carbon that is obtained under given environmental conditions.

In this Master's Thesis, we will focus on the maximum power principle and we will determine if it can be used to predict flow regimes in shallow reservoirs for a given configuration.

3 Meandering flows in shallow rectangular reservoirs: Impact of geometrical parameters

3.1 Introduction

In this section, the study focuses on meandering flows. Contrary to symmetric flows that are fairly well understood in our time, the understanding of phenomena occurring in meandering flows should be improved. The knowledge of this flow pattern will lead to better prediction of deposit patterns and therefore to the improvement of reservoir management.

Peltier et al. (2014a) demonstrated through a dimensional analysis that the meandering jets in rectangular shallow reservoirs can be described based on geometric, hydraulic and fluid parameters. The main characteristics of the jet are its wavelength, its width, both respectively defined by Peltier et al. (2014a) as the characteristic longitudinal and lateral length of the jet and its frequency which is included in the dimensionless number St called Strouhal number and expressed as follows:

$$St = f\frac{H}{V} \tag{3}$$

with f the vortex emission frequency, H the water depth and V the flow velocity.

In its dimensional analysis, Peltier et al. (2014a) showed that these three characteristics of the jet can be expressed as a function of the Shape Factor, the friction number and the Froude number:

$$\left(St, \frac{\Lambda_x}{H}, \frac{\Lambda_y}{H}\right) = f(SF, S, F) \tag{4}$$

In order to obtain non-dimensional numbers, the two characteristic lengths Λ_x and Λ_y were normalized by the water depth H. The water level was chosen instead of the width because of observations made by Dracos et al. (1992).

The influence of the friction number and the Froude number on the main characteristics of the jet has already been studied by Peltier et al. (2014a) but not the impact of the Shape Factor. This first part will therefore focus on the incidence of geometrical parameters such as the width or the length of the reservoir on the three characteristics of the jet.

At first, the experimental set-up will be detailed and methods used will be explained. A first configuration will be then used to validate the experimental protocol followed by Peltier et al. (2014a,b,c). The influence of geometric parameters (length and width of the reservoir) on main characteristics of meandering flows will finally be discussed based on two other configurations.

For each configuration, Large-Scale Particle Image Velocimetry (LSPIV) will be performed to determine instantaneous surface velocity fields and a Proper Orthogonal Decomposition (POD) will be applied on these fields in order to determine the spatial and temporal modes.

3.2 Experimental set-up

3.2.1 Experimental flume

Experiments were performed in a flume situated in the laboratory of engineering hydraulics of the University of Liège (ULg) in Belgium.The experimental protocol is the same as the one proposed by Peltier et al. (2014a,b,c). The experimental shallow reservoir is displayed in Figure 3 and 4. It consists in a horizontal flume of 10.40 m long and 0.98 m wide, composed of movable blocks that can be rearranged in order to build different geometries of rectangular reservoirs. All the surfaces are made of glass, except for the bottom of the flume which is in polyvinyl chloride PVC and the converging section (metallic sheets).

The flow enters first in a stilling basin and passes by a porous screen which prevents fluctuations in water level and allows to establish faster a fully developed velocity profile. The flow is then contracted in the inlet channel which is 2.00 m long and 0.08 m wide. When the flow enters in the reservoir, it expands to the width of the reservoir $B = b + 2\Delta B$. The flow is again contracted at the outlet channel which has the same width as the inlet channel. The length of the outlet channel depends on the experiment performed. The flume is ended by a tailgate.
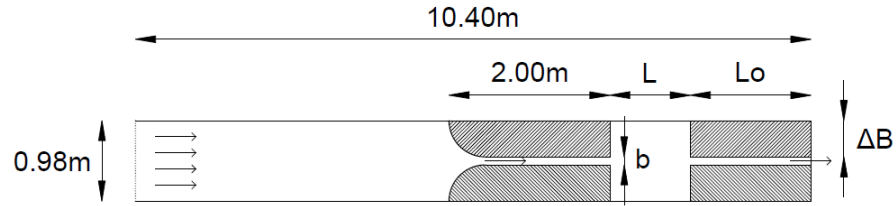
FIGURE 3 – Sketch of the experimental reservoir and representation of main geometric notations
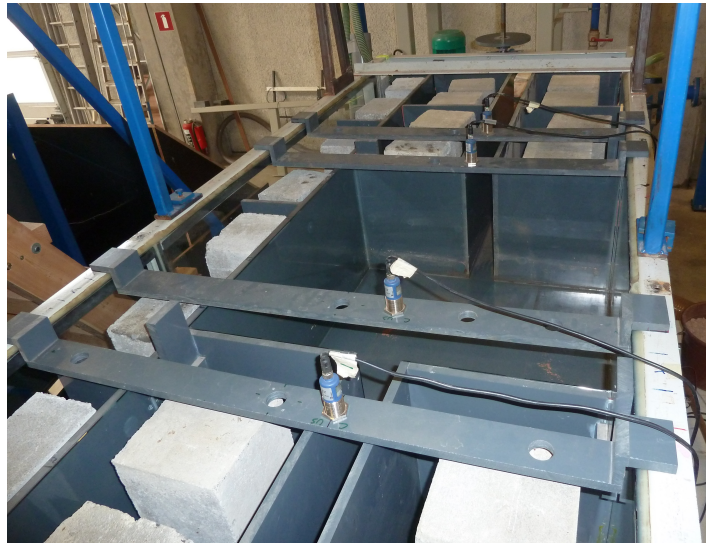
FIGURE 4 – Photo of the experimental reservoir

3.2.2 Measuring instruments

3.2.2.1 Discharge measurement

The discharge Q is evaluated through an electromagnetic flow-meter (uncertainty of 0.025 L/s) which is placed on the pipe that links the downstream tank to th upstream tank (Figure 5).

FIGURE 5 – Photo of the electromagnetic flow-meter

The water levels are kept constant in both reservoirs in order to avoid any discharge variations. The pump is indeed regulated through a pressure sensor, which requires that the differential within the pump is constant.

3.2.2.2 Water depth measurements

Four ultrasonic probes (uncertainty of 0.02 cm) were used (see Figure 6) to measure the water depth. At the beginning of each day devoted to experimental testing, ultrasonic probes were calibrated.
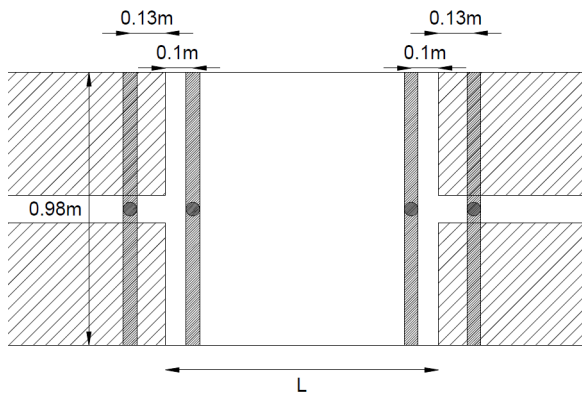
FIGURE 6 – Sketch (left) of the arrangement of the probes - The *black circles* represent the probes and the *hatched rectangles* are the supports on which they are installed - and photo (right) of the two probes located upstream of the reservoir

3.2.2.3 Measurements of velocity fields

Knowing the size of the experiments and the experimental set-up, only the flow surface can be used to estimate the velocity fields.Peltier et al. (2014c) showed that this approach gives a reasonable representation of the large-scale instabilities. These surface dynamics are evaluated using a method called Large-Scale Particle Image Velocimetry (LSPIV).

Method principle

As explained by Muste et al. (2010), the Particle Image Velocimetry (PIV) is based on four steps that lead ultimately in obtaining the velocity fields in the reservoir:

  – « *Flow visualization,*
  – *Illumination,*
  – *Image recording and*
  – *Image processing* » Muste et al. (2010)

The LSPIV is an extension of the PIV. However, contrary to PIV taking place in laboratory because of specific conditions concerning light and tracers, the LSPIV is conducted in natural light and allows to study a larger area. This technique is also less expensive.

The flow dynamics extracted from the LSPIV velocity fields are assumed to be acceptable in terms of representation of instability phenomena as explained by Peltier et al. (2014c) in his article. It is for all these reasons that this technique is chosen.

A Cartesian coordinate system is used in which:

  – x is the longitudinal direction and is equal to zero immediately downstream from the inlet channel
  – y is the lateral direction and starts at the right bank of the reservoir
  – z is the vertical direction and equals zero at the bottom of the reservoir.

Experimental procedure

In order to avoid having too much light reflection, tarpaulins are installed around the reservoir as can be seen in Figure 7.

FIGURE 7 – Tarpaulins around the reservoir

Sawdust of 2 mm of mean diameter are widespread on the surface of the flow before the inlet channel and the reservoir is video-recorded using a commercial video-camera (Canon© HD-HG20) at a rate of 25 Hz during 10 min.

First, images are extracted from the video-sequence using ffmpeg (http://www.ffmpeg.org/). These one are then corrected in two ways: Firstly, they are filtered using the recommendation of Thielicke and Stamhuis (2014). Secondly, a lens correction is applied using Imagemagick (http://www.imagemagick.org/) because images obtained with the camera are distorted (The line of the image are curved). After that, orthorectification of the images is carried out and therefore one pixel is equal to a square of 1 mm side. Finally, the PIV analysis is performed on a mesh with cells of $1cm \times 1cm$.

3.3 Methods

3.3.1 Proper orthogonal decomposition (POD)

The Proper Orthogonal Decomposition is used after obtaining the velocity fields by LS-PIV to determine the modes corresponding to coherent structures that develop in the flow. This method is used because it allows to study unsteady flows in contrast to parameters such as the average speed that determines an average and does not take into account the unsteady phenomenon.

The equations on which this method is based are detailed in the paper of Peltier et al. (2014c).

3.3.2 Propagation of uncertainties

The propagation of uncertainties is given by the following formula:

$$G = f(x, y) \Rightarrow \Delta G = \sqrt{\left(\frac{\partial f}{\partial x}\right)^2 \delta x^2 + \left(\frac{\partial f}{\partial y}\right)^2 \delta y^2} \tag{5}$$

The Froude number can be expressed as a function of the discharge and the water depth as follows:

$$F = \frac{U}{\sqrt{gH}} = \frac{Q}{b\sqrt{gH^3}} \tag{6}$$

Based on equation (5), the uncertainty on the Froude number can be written as:

$$\delta F = \sqrt{\left(\frac{1}{b\sqrt{gH^3}}\right)^2 (\delta Q)^2 + \left(-\frac{3Q}{2bH\sqrt{gH^3}}\right)^2 (\delta H)^2 + \left(-\frac{Q}{b^2\sqrt{gH^3}}\right)^2 (\delta b)^2} \tag{7}$$

The friction number and its uncertainty are given by:

$$S = C_f \frac{\Delta B}{8H} \tag{8}$$

$$\delta S = \sqrt{\left(\frac{\Delta B}{8H}\right)^2 (\delta C_f)^2 + \left(\frac{C_f}{8H}\right)^2 (\delta \Delta B)^2 + \left(-\frac{C_f \Delta B}{8H^2}\right)^2 (\delta H)^2} \tag{9}$$

The uncertainty of the Shape Factor SF writes :

$$\delta SF = \sqrt{\left(\frac{\partial SF}{\partial L}\right)^2 \delta L^2 + \left(\frac{\partial SF}{\partial b}\right)^2 \delta b^2 + \left(\frac{\partial SF}{\partial \Delta B}\right)^2 \delta \Delta B^2} \tag{10}$$

$$= \sqrt{\left(\frac{1}{\Delta B^{0.6}b^{0.4}}\right)^2 \delta L^2 + \left(\frac{-2L}{5\Delta B^{0.6}b^{7/5}}\right)^2 \delta b^2 + \left(\frac{-3L}{5\Delta B^{8/5}b^{0.4}}\right)^2 \delta \Delta B^2} \tag{11}$$

The uncertainty of the normalized characteristic lengths can be expressed as :

$$\delta \frac{\Lambda_x}{H} = \sqrt{\left(\frac{1}{H}\right)^2 (\delta\Lambda_x)^2 + \left(-\frac{\Lambda_x}{H^2}\right)^2 (\delta H)^2} \tag{12}$$

$$\delta \frac{\Lambda_y}{H} = \sqrt{\left(\frac{1}{H}\right)^2 (\delta\Lambda_y)^2 + \left(-\frac{\Lambda_y}{H^2}\right)^2 (\delta H)^2} \tag{13}$$

3.4 Validation of the protocol

3.4.1 Introduction

The main purpose of this first configuration is to validate the protocol followed by Peltier et al. (2014a,b,c). To do this, a previous studied configuration is reproduced. The experiments were performed for four discharges and in each case, the velocity fields were measured by Large Scale Particle Image Velocity (LSPIV). Modes of meandering flows are then determined by applying a Proper Orthogonal Decomposition (POD) on the corresponding velocity fields.

Before discussing the results, a study of uncertainties is first carried out to know if the differences between the values obtained by Peltier et al. (2014a,b,c) and those with present data are within these uncertainties. An analysis of the results obtained for the main characteristics of the jet defined by Peltier et al. (2014a) in its dimensional analysis which are the normalized characteristic lengths and the Strouhal number is then realized. Finally, the spatial modes and the temporal coefficients based on data collect by Peltier et al. (2014a,b,c) and present data are compared.

3.4.2 Data set

In this configuration, the sudden expansion width ΔB is equal to 0.45 m which leads to a total width B of 0.98 m. The length of the reservoir L is set to 1 m and for the outlet channel, it is equal to 1.5 m. With all of these geometric parameters, the shape factor SF can be calculated :

$$SF = \frac{L}{\Delta B^{0.6} b^{0.4}} = 4.43 \tag{14}$$

Four discharge (and so four water depth associated) were chosen so that the Froude number F is greater than 0.21. Under these conditions (see State of the art), the observed flows are meandering. The main flow characteristics which are determined with the equations below obtained with data collected by Peltier et al. (2014a,b,c) and present data are respectively listed in Table 1 and 2.

$$U_{in} = \frac{Q}{bH}; F = \frac{U_{in}}{\sqrt{gH}}; Re = \frac{4U_{in}}{\nu}\frac{Hb}{b+2H}; S = f\frac{\Delta B}{8H} \tag{15}$$

Discharge Q $[L/s]$	Water depth H $[cm]$	Inlet velocity U_{in} $[m/s]$	Froude number F $[-]$	Reynolds Re $[-]$	Friction number S $[-]$
0.245	1.8	0.17	0.41	8456	0.10
0.501	2.7	0.23	0.44	14878	0.06
1.000	4.2	0.30	0.46	24454	0.03
1.530	5.6	0.35	0.47	32008	0.02

TABLE 1 – Main flow characteristics (data collected by Peltier et al. (2014a,b,c))

Discharge Q [L/s]	Water depth H [cm]	Inlet velocity U_{in} [m/s]	Froude number F [−]	Reynolds Re [−]	Friction number S [−]
0.256	2.1	0.15	0.33	8444	0.09
0.495	3.0	0.20	0.37	14264	0.05
0.749	3.7	0.26	0.43	19547	0.04
1.005	4.3	0.29	0.45	24262	0.03

TABLE 2 – Main flow characteristics (present data)

For a given discharge, values of the different factors listed in both tables are almost identical. The difference comes from the values of the discharges that differ slightly. The values obtained for the Reynolds number Re confirm that the flow is turbulent. These experiments were performed two or three times so as to ensure that there is no hysteresis effect.

For each flow-case, the instantaneous surface velocity fields were obtained using LSPIV. A Proper Orthogonal Decomposition (POD) was then performed on these fields in order to determine the energetic structures in the flow. Finally, a 1D Fourier analysis was applied on temporal modes obtained so as to evaluate the characteristic frequency f_{max}. The same method was performed on spatial modes, more precisely, on the vorticity fields deduced from them, to identify the characteristic lengths of the jet. As defined by Peltier et al. (2014a):

- Λ_x corresponds to the characteristic longitudinal length and is « *the inverse of the wave number corresponding to the maximum of the spectrum of the longitudinal distribution of the vorticity field within an interval of five centimeters on both sides of the reservoir centerline,* » Peltier et al. (2014a)

- Λ_y represents the characteristic lateral length and is « *the mean of the inverses of the wave numbers corresponding to the maximums of the spectrum of the distribution of vorticity in each cross-section.* » Peltier et al. (2014a)

3.4.3 Results and discussion

In Figure 8, the dispersion of the points obtained for each experiment based on the Froude number and the shape factor is shown. These two parameters define the respective domains of occurrence of each type of flow. Thus, the meandering flow can be found in the domain where $F > 0.21$ and $SF < 6.2$ (represented by the horizontal dashed red line). For $F < 0.21$ and $SF < 6.2$, flows are symmetric while the asymmetric flows are defined for $SF > 6.2 - 8.1$ with no restriction on the Froude number value. For $6.2 < SF < 8.1$, instable flows can be observed.
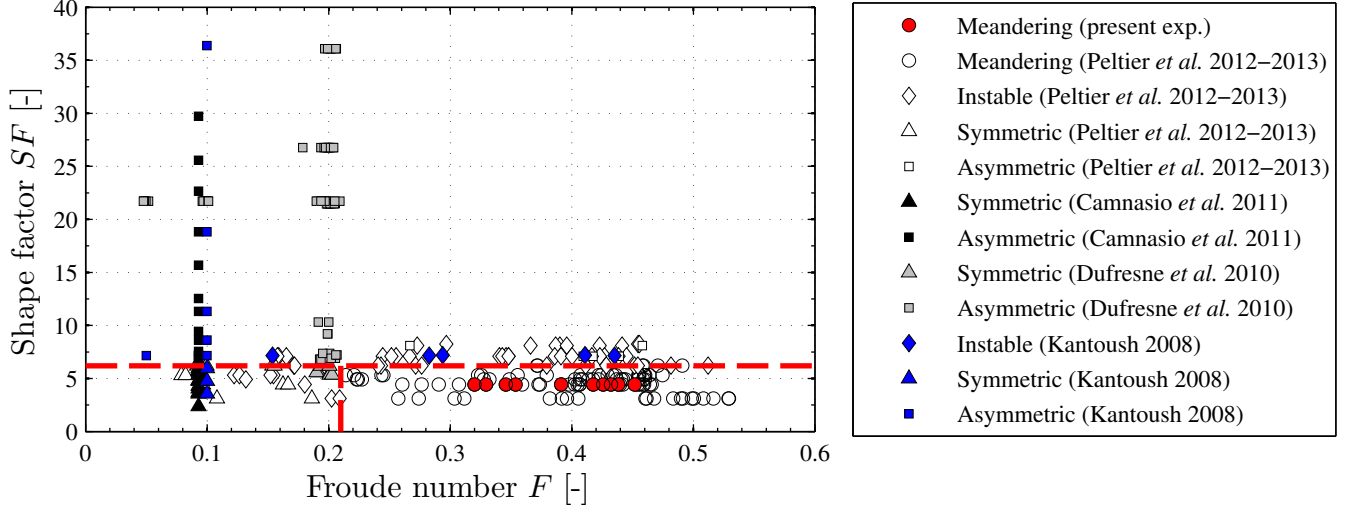
FIGURE 8 – Representation of the different type of flow depending on the Froude number F and shape factor SF. (The horizontal dashed red line corresponds to $SF = 6.2$ and the vertical one is for $F = 0.21$)

3.4.3.1 Domain of existence

In Figure 8, the points corresponding to the same discharge are not located at the same place because of uncertainties related to certain parameters. The uncertainty associated with the discharge is equal to 0.5% of the maximum value of the permissible flow which is here $2L/s$.

$$\delta Q = \frac{0.5}{100} \times 2 = 0.01 L/s \tag{16}$$

The uncertainty of the water depth is taken equal to 0.2 mm given by the constructor. Another alternative would be to consider $\delta H = 0.01 H$. However, this approach is very safe and is not selected.

The set of variables and uncertainties obtained based on equations developed in section 3.3.2 are summarized in Table 3 and are evaluated based on :

$$\delta \Delta B = \delta L = 0.005 m \;\; \& \;\; \delta b = 0.001 m \;\; \& \;\; \delta f = 0.001 \tag{17}$$

14

| Q | δQ | H | δH | F | δF | S | δS |
$[L/s]$	$[L/s]$	$[cm]$	$[cm]$	$[-]$	$[-]$	$[-]$	$[-]$
0.25	0.01	2.1	0.02	0.33	0.0145	0.09	0.003
0.5	0.01	3.0	0.02	0.37	0.0098	0.05	0.002
0.75	0.01	3.7	0.02	0.43	0.0084	0.04	0.002
1.00	0.01	4.3	0.02	0.45	0.0078	0.03	0.001

TABLE 3 – Variables and uncertainties

The uncertainty of the SF given by equation (11) equals:

$$\delta SF = 0.0431 \tag{18}$$

By comparing the results obtained with data collected by Peltier et al. (2014a,b,c) and present data (Tables 1 and 2, it can be seen that the difference between the heights obtained for a given discharge is greater than the uncertainty. This difference probably comes from a repeatability error that may be due to the height at which the probes are located, the bottom friction or another factor.

Concerning the uncertainty of the characteristics lengths, they varies as a function of the water depth H bewteen :

$$\delta \Lambda_x = 0.0116 - 0.0238 \tag{19}$$
$$\delta \Lambda_y = 0.0116 - 0.0238 \tag{20}$$

3.4.3.2 Normalized characteristic lengths

The evolution of the normalized characteristic lengths Λ_x/H and Λ_y/H according to the Froude number F and the friction number S are represented in Figure 9 and 10.
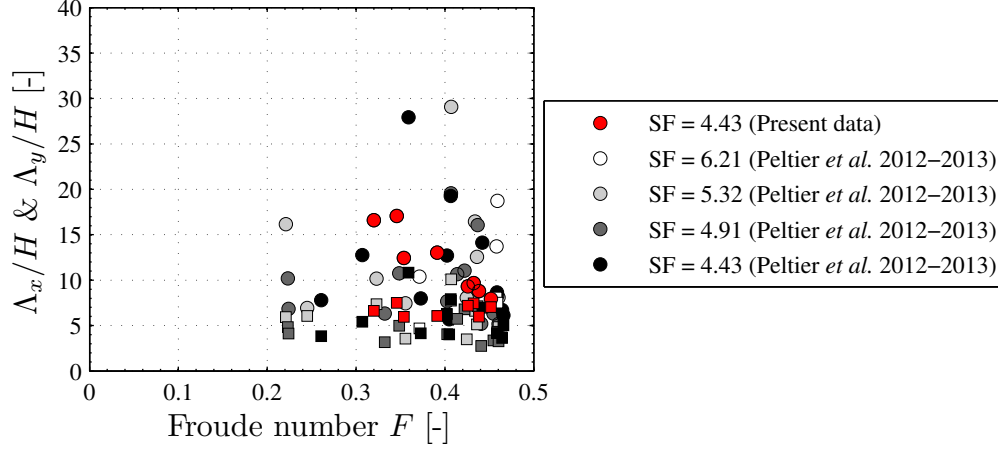
FIGURE 9 – Evolution of the normalized characteristic lengths Λ_x/H ($\bigcirc$) and Λ_y/H ($\square$) depending on the Froude number F

As shown previously by Peltier et al. (2014a), no clear relationship appears between the normalized characteristic lengths and the Froude number. Conversely, the correlation between the characteristic lengths and the friction number S is clearly visible. In both cases, the relationship between the variables was expressed using the least square method as follows:

$$\frac{\Lambda_x}{H} = 145 \times S + 2.4 \; (R^2 = 0.85) \tag{21}$$

$$\frac{\Lambda_y}{H} = 20 \times S^{0.45} \; (R^2 = 0.62) \tag{22}$$

R^2 is the coefficient of determination that indicates the quality of the regression (between 0 and 1).
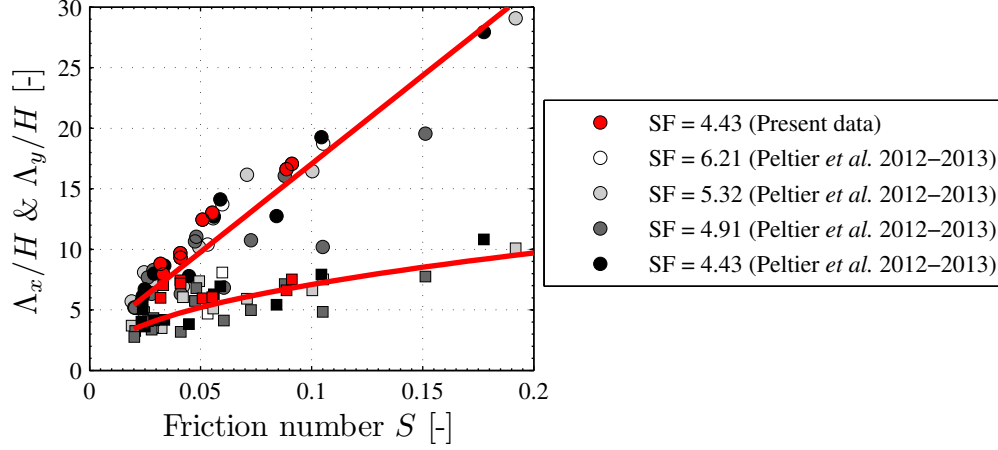
FIGURE 10 – Normalized characteristic lengths Λ_x/H ($\bigcirc$) and Λ_y/H ($\square$) plotted against the friction number S

In this Figure, the present data follow the same trend. By adding these points, the regression lines become:

$$\frac{\Lambda_x}{H} = 147 \times S + 2.7 \ (R^2 = 0.87) \tag{23}$$

$$\frac{\Lambda_y}{H} = 21 \times S^{0.47} \ (R^2 = 0.55) \tag{24}$$

The coefficients obtained are similar to those determined by Peltier et al. (2014a).

In Figure 11, the evolution of the ratio of the characteristic lengths Λ_x/Λ_y according to the friction number S is plotted. The observations of Peltier et al. (2014a) highlight a linear correlation for $S > 0.07$ (Frictional zone) which can be written as follows:

$$\frac{\Lambda_x}{\Lambda_y} = 6.83 \times S + 1.61 \ (R^2 = 0.65) \tag{25}$$
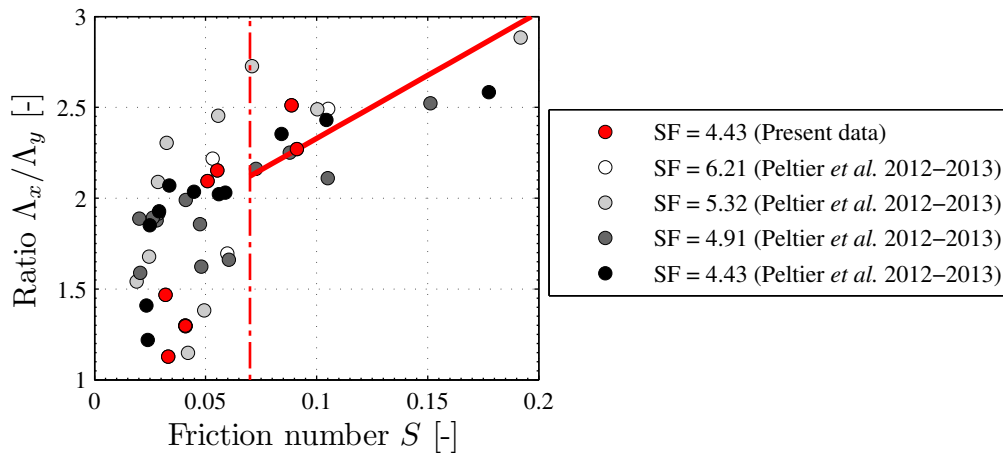
FIGURE 11 – Representation of the ratio of the characteristic lengths Λ_x/Λ_y according to the friction number S

17

Considering the data, the regression line is given by:

$$\frac{\Lambda_x}{\Lambda_y} = 6.94 \times S + 1.63 \ (R^2 = 0.61) \tag{26}$$

The slope and constant obtained are similar to those of equation (25).

3.4.3.3 Strouhal number

In his paper, Peltier et al. (2014a) shows that there is no relationship between the Strouhal number St, the Froude number F and the shape factor SF. However, a correlation between the Strouhal number St and friction number S was demonstrated. The relation between these two variables is shown in Figure 12 and can be expressed as:

$$St = 0.004 \times S^{-0.776} \ (R^2 = 0.66) \tag{27}$$
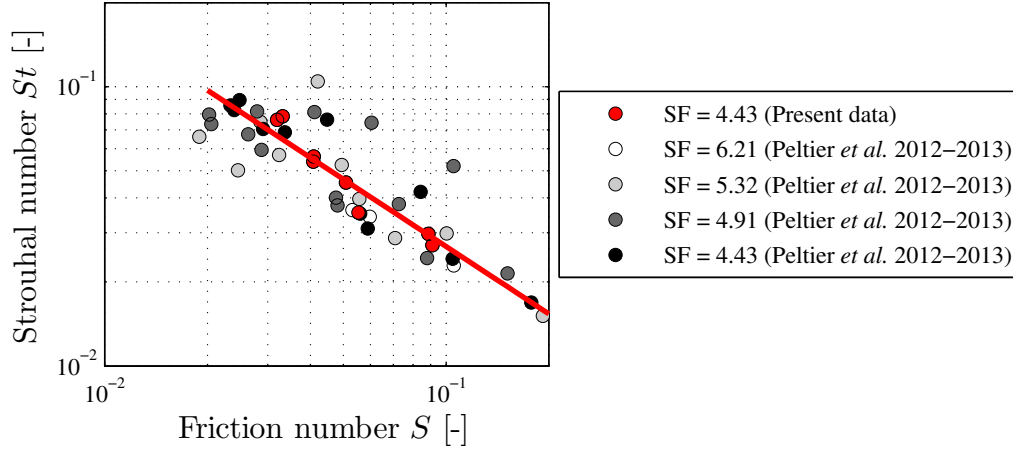
FIGURE 12 – Strouhal number St plotted with respect to the friction number S

With the present data, it writes:

$$St = 0.004 \times S^{-0.8} \ (R^2 = 0.74) \tag{28}$$

The constant and the exponent used in the regression and obtained with data from Peltier et al. (2014a,b,c) and present data are very similar.

3.4.4   POD analysis - comparaison

The POD analysis was realized on each performed experimental flow. 10000 snapshots were used to obtain the eigenvalues λ_m (10000). Their value decreases as the mode number m increases. Thus, the first modes with a high eigenvalue contributes more to the representation of motions while others have a lower contribution.

In the following, a comparison between data collected by Peltier Y. (2012-2013) and present data is performed for a discharge Q of 0.50 L/s. The same study is made for Q equals to 0.25 L/s and is Appendix A.1.1. Only the five first modes will be considered. Indeed, the sixth or the seventh eigenvalue respectively represents 6.5% and 5.3% of the first one, this means that the corresponding modes have a lower contribution to the representation of motions with respect to the first mode.

3.4.4.1   Temporal coefficients

The temporal coefficients obtained from the eigenvectors of the five first modes are represented in Figure 13 for a discharge Q of 0.50 L/s, and this for the data collected by Peltier Y. (2012-2013) and the present data in order to compare them.
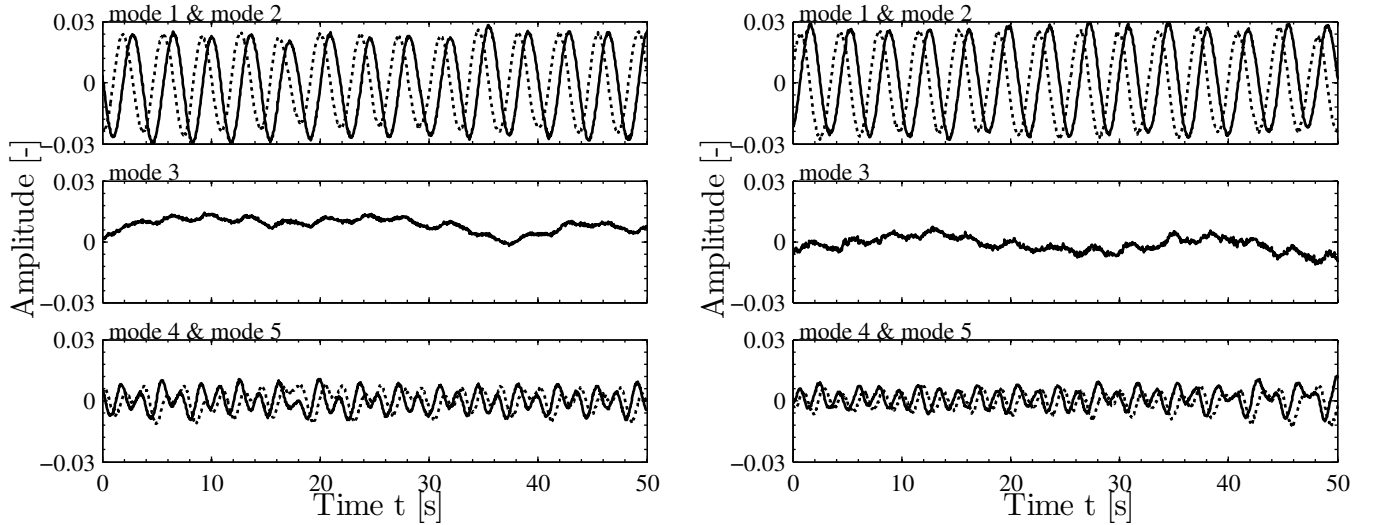
FIGURE 13 – Representation of the temporal coefficients of the five first mode corresponding to $Q = 0.50$ L/s for Peltier's data (left) and present data (right) - The *solid lines* represent odd modes and the *dotted lines* even modes

On each graph, the first and the second mode are similar but phase-shifted in time. Thus, it is possible to conclude that they are paired as explained by Peltier et al. (2014c). The following modes ($m > 2$) are characterized by smaller and less regular amplitudes.

In order to compare the modes obtained, a method called Modal Assurance Criterion (MAC) proposed by Andrianne T. (see Andrianne and Dimitriadis (2012)) is used. The MAC is evaluated based on mode i of the first data and mode j of the second data.

$$MAC\left(x_{(i)}^1, x_{(j)}^2\right) = \left(\frac{{x_{(i)}^1}^T x_{(j)}^2}{||x_{(i)}^1||||x_{(j)}^2||}\right)^2 \tag{29}$$

where $x_{(i)}^1$ and $x_{(i)}^2$ are vectors containing the temporal coefficients of mode i respectively obtained with the data collected by Peltier et al. (2014a,b,c) and present data.

It varies between 0 and 1, a unitary value indicates a perfect match. The results obtained for the first 10 modes are shown in Figure 14.
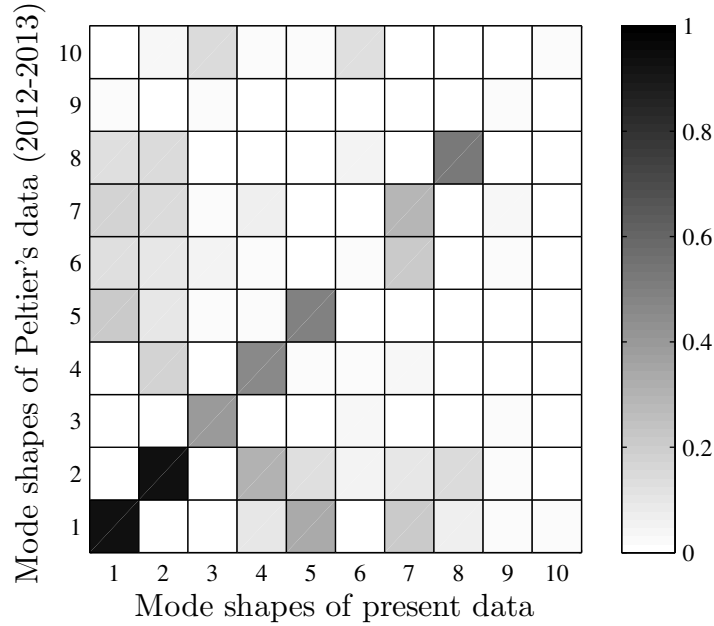
FIGURE 14 – Comparison between Peltier's data (2012-2013) and present data using MAC matrix

In this figure, it can be seen that the correlations being on the diagonal, i.e. those comparing the modes with the same number, are almost all nonzero. In particular, the first two modes whose energy is the highest have a correlation close to unity. Relations between different modes are probably due to uncertainty or precision errors of the results obtained using the LSPIV.

3.4.4.2 Spatial modes

The first five spatial modes corresponding to a discharge Q of 0.50 L /s are displayed in Figure 15 for Peltier's data (2012-2013) and in Figure 16 for present data.

In order to identify the different coherent structures in the spatial modes, the definition of a vortex established by Kolár (2007) and previously used by Peltier et al. (2014c) is applied. In this approach, the vortex region is characterized by a non-zero residual vorticity when the 2D principal rate of strain s is lower than the 2D vorticity-tensor component w. The residual vorticity can be evaluated based on the following equations:

$$w_{res} = \begin{cases} sgn(w) \left(|w| - |s| \right) & \text{when } |s| < |w| \\ 0 & \text{otherwise} \end{cases} \tag{30}$$

with

$$|s| = \frac{1}{2} \sqrt{4 \left(\frac{\partial \phi_{xm}}{\partial x} \right)^2 + \left(\frac{\partial \phi_{xm}}{\partial y} + \frac{\partial \phi_{ym}}{\partial x} \right)^2} \tag{31}$$

$$w = \frac{1}{2} \left(\frac{\partial \phi_{ym}}{\partial x} - \frac{\partial \phi_{xm}}{\partial y} \right) \tag{32}$$

where ϕ_{xm} and ϕ_{ym} are respectively the longitudinal and the lateral component of the mth spatial mode.

On each figure, the same conclusion as the one made for temporal modes concerning the similarity between the first and second mode which are simply phase-shifted can be drawn.

The coherent structures observed for the first and second spatial modes obtained with Peltier's data (2012-2013) and present data are similar. However, the colors used to represent the vorticity are different. This comes from the choice of the first mode. If in one case, the temporal coefficients and the spatial modes are respectively positive and negative, it is possible that in another case, their signs are reversed.
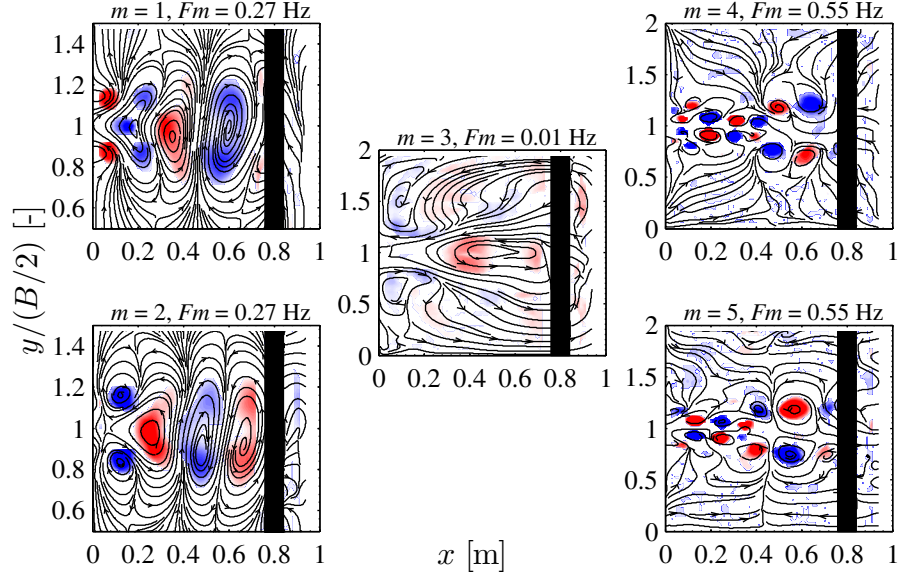
FIGURE 15 – Representation of the first five spatial modes for Q equals to 0.50 L/s based on Peltier's data (2012-2013) - The *black rectangle* corresponds to a blank zone during the measurement - When the vorticity is negative, it is represented in blue while it is in red when it is positive
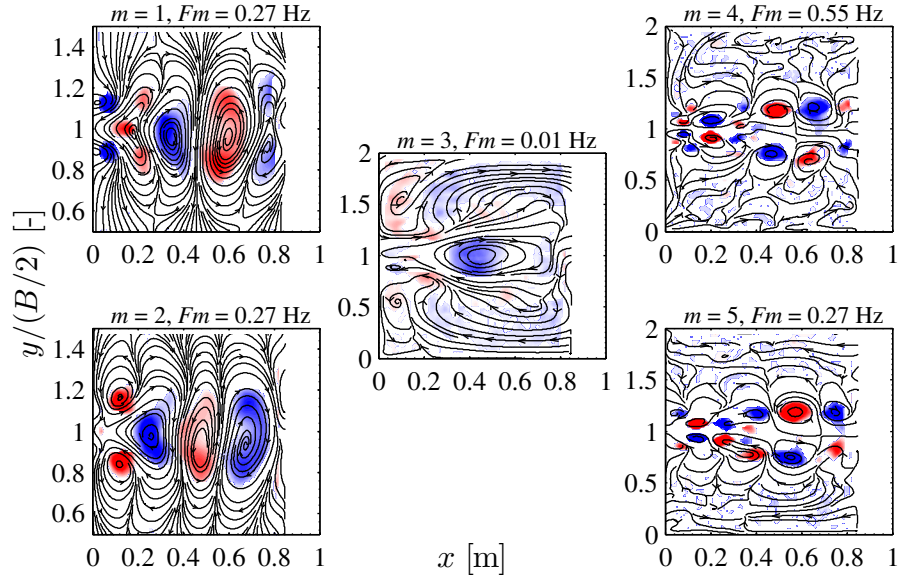
FIGURE 16 – Representation of the first five spatial modes for Q equals to 0.50 L/s based on present data - The *empty area* corresponds to an inaccessible area due to the camera position

3.4.5 Conclusion

The experimental protocol followed by Peltier et al. (2014a,b,c) is validated for the present experiments. Geometrical data of a previous configuration were used to perform the experimental tests. For each meandering flow obtained, the instantaneous surface velocity field was measured and a Proper Orthogonal Decomposition was performed on these fields in order to determine characteristic such as the frequency or the two characteristic lengths (Longitudinal and lateral).

The normalized characteristic lengths of the meandering jet and Strouhal number determined using the frequency were then compared to the Froude number and to the friction number S for various factor shape SF of the reservoir. The data obtained allow us to confirm the conclusions made by Peltier et al. (2014a), namely that there is no relationship between the three characteristic parameters and the Froude number, but that there is a correlation with the number of friction S.

The five first temporal coefficients and spatial modes obtained with data collected by Peltier et al. (2014c) and present data were then compared. In the case of spatial modes, a visual comparison was made whereas for the temporal modes, a quantitative method called Modal Assurance Criterion (MAC) was used. This allowed us to see that the first two modes which are the most energetic were highly similar.

In the end, based on the overall results, we can validate the experimental protocol followed by Peltier et al. (2014a,b,c).

3.5 Effects of varying the expansion ΔB and the length L of the reservoir

3.5.1 Introduction

The experimental protocol being validated, three configurations were then studied to determine the influence of geometric parameters on meandering flows developing in the reservoir, the first one corresponding to the configuration used to validate the experimental protocol in the previous section.

In the second configuration, the width of the reservoir is changed but the length is kept constant compared to the one of configuration studied in the previous section. This geometry leads to a different Shape Factor SF.

In the third configuration, the reservoir width is equal to the one of the second configuration but the length is modified in order to obtain the same Shape Factor SF as the one of the configuration studied in the previous section.

Thus, the influence of the expansion ΔB, the length L but also the scale effects (Same SF but different ΔB and L) can be studied.

On each configuration, various discharges and tailgates were used. Large-Scale Particle Image Velocimetry (LSPIV) was performed to determine velocity fields. Based on them, modes of meandering flows were then evaluated by using a Proper Orthogonal Decomposition (POD).

3.5.2 Data set

Three configurations are considered here in order to analyze the influence of the geometric parameters which are the width and the length of the reservoir:

– The first configuration is actually the validating configuration,

– In the second configuration, the lateral expansion ΔB of the reservoir is reduced compared to the one of the first configuration. The width is an important parameter since in the validation part, it was shown that there was a relationship between the normalized characteristic lengths and the friction number which depends on the lateral expansion ΔB and the friction coefficient f. The latter is difficult to control and so, changing the lateral expansion is relevant.

– For the third configuration, ΔB is equal to the one of the second configuration and the length of the reservoir is modified in order to obtain the same shape factor as the one of the validating configuration.

The main geometrical characteristics of the three experimentally tested configurations are listed in Table 4. In order to facilitate understanding thereafter, the geometric parameters changed from the initial configuration are given in brackets.

	Length L [m]	Width B [m]	Expansion width ΔB [m]	Shape Factor SF [-]
Config.1 (Validation)	1	0.98	0.45	4.43
Config.2 (ΔB)	1	0.78	0.35	5.16
Config.3 ($\Delta B/L$)	0.86	0.78	0.35	4.43

TABLE 4 – Main geometrical characteristics of the two configurations

For each configuration, three different crest heights (gate free, at 2.75cm and at 3.75cm) were used in order to obtain various water depths for a given discharge. For the first crest height (gate free), five different discharges were used whereas only four were tested for the other two crest heights. For each experiment, ascent and descent of discharges were performed to check that there was no hysteresis effect. The results obtained for each experiment such as the Froude number, friction and Reynolds number are presented in Table 5 and Table 6.

Geometry			Hydraulic conditions				
L [m]	ΔB [m]	Gate	Q [L/s]	H [cm]	F [-]	S [-]	$Re \times 10^{-2}$ [-]
1.00	0.35	Free	0.124	1.7	0.23	0.11	43.93
1.00	0.35	Free	0.251	2.2	0.32	0.07	81.63
1.00	0.35	Free	0.503	3.1	0.37	0.04	142.1
1.00	0.35	Free	0.995	4.4	0.44	0.03	237.98
1.00	0.35	Free	1.518	5.4	0.48	0.02	321.68
1.00	0.35	Free	1.514	5.6	0.46	0.02	316.12
1.00	0.35	Free	1.003	4.4	0.43	0.03	237.54
1.00	0.35	Free	0.496	3.1	0.37	0.04	140.24
1.00	0.35	Free	0.252	2.2	0.31	0.07	81.41
1.00	0.35	Free	0.112	1.3	0.29	0.13	41.93
1.00	0.35	2.75cm	0.252	4.0	0.13	0.04	63.29
1.00	0.35	2.75cm	0.499	4.7	0.19	0.03	114.35
1.00	0.35	2.75cm	1.008	5.9	0.28	0.02	203.85
1.00	0.35	2.75cm	1.533	7.0	0.33	0.02	280.09
1.00	0.35	2.75cm	1.063	5.9	0.29	0.02	214.27
1.00	0.35	2.75cm	0.504	4.7	0.20	0.03	115.82
1.00	0.35	2.75cm	0.263	4.1	0.13	0.04	65.14
1.00	0.35	3.75cm	0.258	5.2	0.09	0.03	56.23
1.00	0.35	3.75cm	0.509	5.9	0.14	0.02	103.17
1.00	0.35	3.75cm	1.006	7.5	0.20	0.02	175.19
1.00	0.35	3.75cm	1.566	8.8	0.24	0.01	244.82

TABLE 5 – Hydraulic conditions obtained for the second configuration (ΔB) and for three different crest heights

Geometry			Hydraulic conditions				
L [m]	ΔB [m]	Gate	Q [L/s]	H [cm]	F [-]	S [-]	$Re \times 10^{-2}$ [-]
0.86	0.35	Free	0.124	1.4	0.29	0.12	45.61
0.86	0.35	Free	0.256	2.0	0.36	0.07	85.15
0.86	0.35	Free	0.502	2.8	0.43	0.05	147.43
0.86	0.35	Free	1.001	4.1	0.48	0.03	247.81
0.86	0.35	Free	1.537	5.3	0.50	0.02	330.32
0.86	0.35	Free	0.999	4.1	0.49	0.03	248.12
0.86	0.35	Free	0.516	2.9	0.43	0.04	150.73
0.86	0.35	Free	0.253	2.0	0.35	0.07	83.94
0.86	0.35	Free	0.130	1.4	0.30	0.12	47.63
0.86	0.35	2.75cm	0.264	4.3	0.12	0.04	63.30
0.86	0.35	2.75cm	0.507	4.9	0.18	0.03	113.31
0.86	0.35	2.75cm	1.007	6.1	0.27	0.02	199.75
0.86	0.35	2.75cm	1.492	7.1	0.32	0.02	270.11
0.86	0.35	2.75cm	1.013	6.1	0.27	0.02	199.98
0.86	0.35	2.75cm	0.503	5.0	0.18	0.03	112.09
0.86	0.35	2.75cm	0.256	4.3	0.12	0.04	62.73
0.86	0.35	3.75cm	0.257	5.2	0.09	0.03	55.88
0.86	0.35	3.75cm	0.506	5.9	0.14	0.02	102.58
0.86	0.35	3.75cm	1.001	7.0	0.22	0.02	182.68
0.86	0.35	3.75cm	1.484	8.0	0.26	0.01	247.80
0.86	0.35	3.75cm	1.017	7.0	0.22	0.02	185.38
0.86	0.35	3.75cm	0.506	5.9	0.14	0.02	102.43
0.86	0.35	3.75cm	0.260	5.2	0.09	0.03	56.30

TABLE 6 – Hydraulic conditions obtained for the third configuration (ΔB) and for three different crest heights

For all experiments with increasing discharge (ascent), the procedure used is the same as for the first configuration :

- Evaluation of velocity fields using Large-Scale Particle Image Velocimetry (LSPIV).

- Determination of the energetic structures, spatial and temporal modes applying a Proper Orthogonal Decomposition (POD) on the velocity fields obtained in the previous step.

- Application of 1D Fourier analysis on temporal modes to evaluate the characteristic frequency f_{max} and on spatial modes to determine the characteristic lengths of the jet Λ_x and Λ_y.

3.5.3 Results and discussion

3.5.3.1 Domain of existence

The flows obtained for all experiments are shown as a function of the Froude number F and the Shape Factor SF in Figure 17. Most of flows are meandering. Symmetric and unstable flows were also obtained but no asymmetric due to the fact that the shape factor of the two configurations does not exceed 6.2.
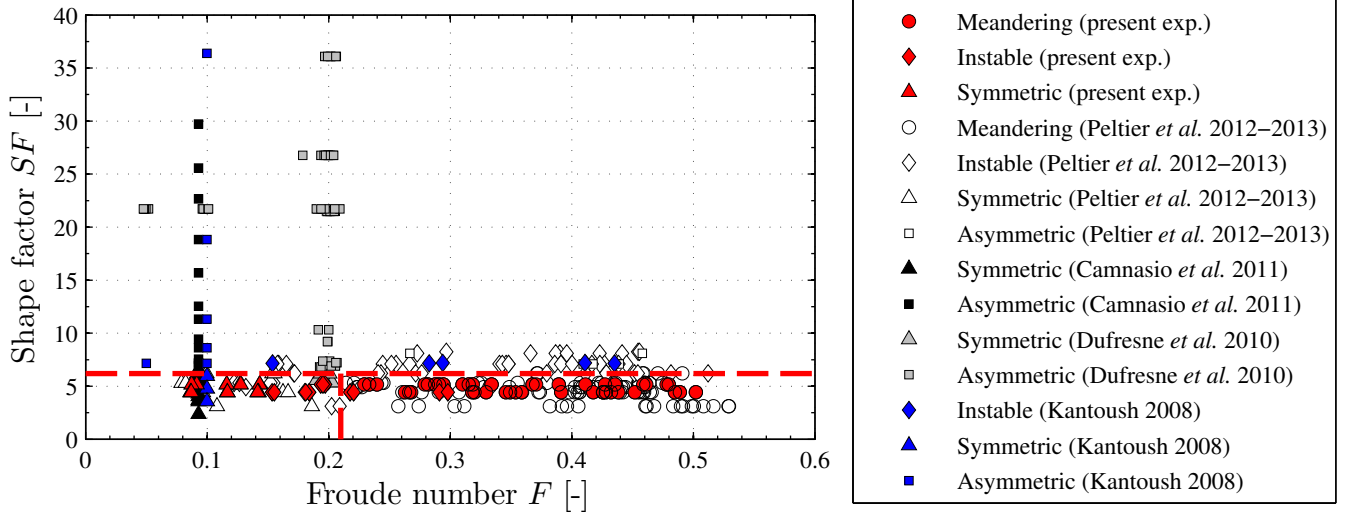

FIGURE 17 – Representation of the different type of flow depending on the Froude number F and shape factor SF. (The horizontal dashed red line corresponds to $SF = 6.2$ and the vertical one is for $F = 0.21$)

A zoom for viewing the different flow regimes occurring around boundaries is displayed in Figure 18.

The boundary $F = 0.21$ correctly separate the symmetrical and meandering flows. In the literature, the unstable regime is defined by the following conditions :

$$\begin{aligned} F \sim 0.21 \ \ & \ \ \ \ \ \ \ \ \ \ \ SF < 6.2 \\ F > 0.21 \ \ & \ \ 6.2 < SF < 8.1 \end{aligned} \tag{33}$$

However, considering the first condition, in Figure 18, it can be seen that there are not only points located at $F \sim 0.21$ but that the zone extends from 0.1 to 0.21. For the second condition, the domain $6.2 < SF < 8.1$ is too restrictive since points corresponding to unstable regime can be found for $SF = 3.1$.

All these observations shows that the boundaries between the different flow regimes are not yet well defined. This point will need to be studied in detail in the future.
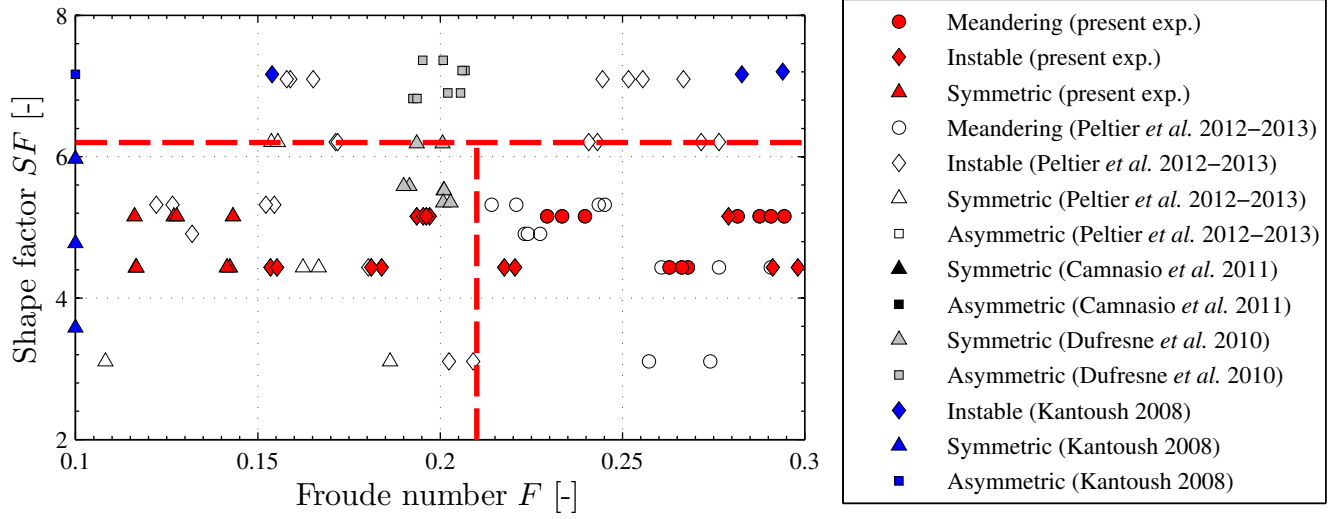
FIGURE 18 – Zoom on the different type of flow depending on the Froude number F and shape factor SF. (The horizontal dashed red line corresponds to $SF = 6.2$ and the vertical one is for $F = 0.21$)

3.5.3.2 Normalized characteristic lengths

The evolution of the normalized characteristic lengths Λ_x/H and Λ_y/H is plotted against the Froude number F respectively in Figure 19 and Figure 20.
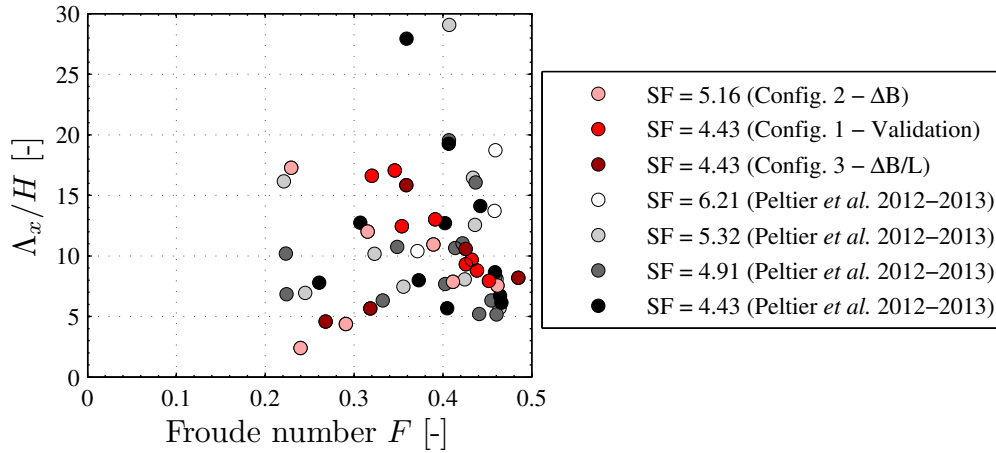
FIGURE 19 – Normalized characteristic length Λ_x/H plotted against the Froude number F
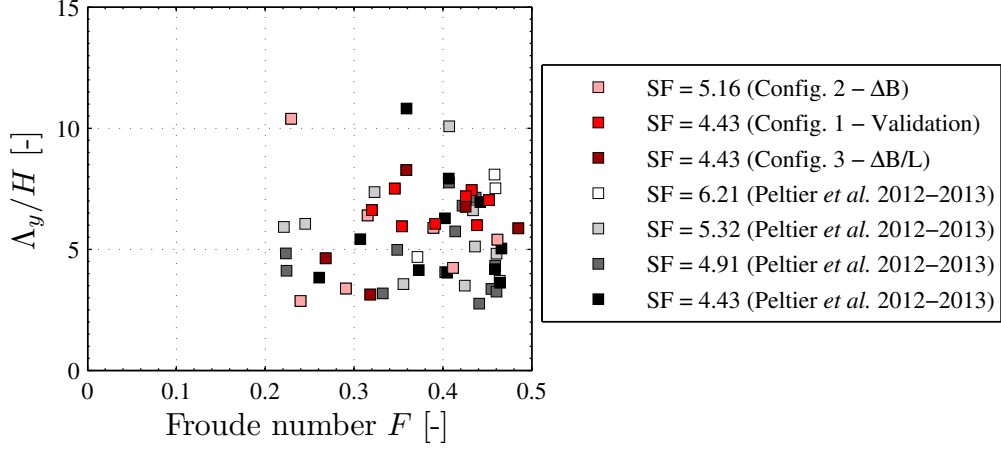
FIGURE 20 – Normalized characteristic length Λ_y/H plotted against the Froude number F

In both Figures, no clear correlation can be found between the normalized characteristic lengths and the Froude number.

In Figures 21 and 22, the normalized characteristic lengths Λ_x/H and Λ_y/H are displayed as a function of the friction number S.
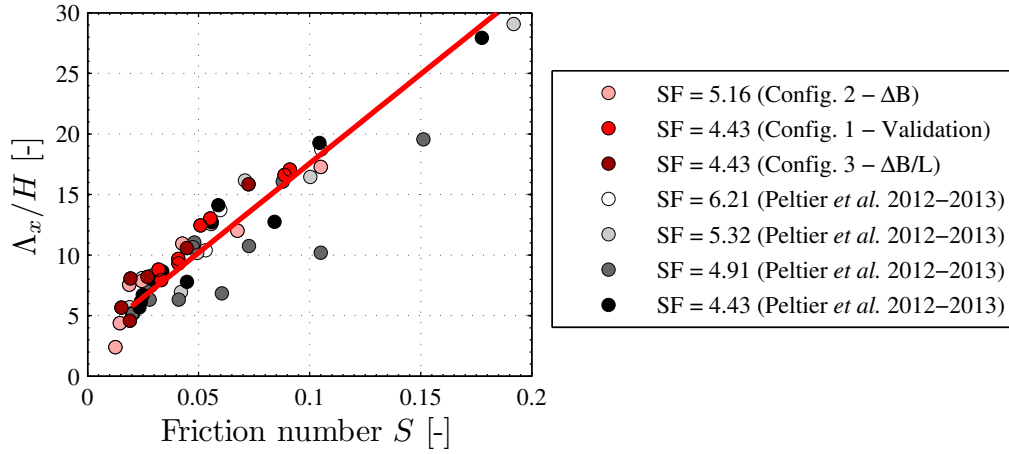
FIGURE 21 – Normalized characteristic length Λ_x/H plotted against the friction number S
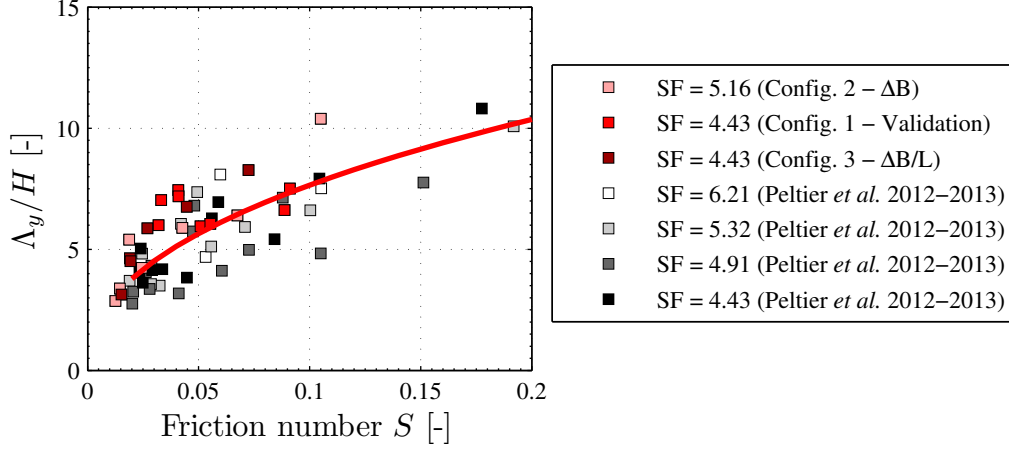
FIGURE 22 – Evolution of the normalized characteristic length Λ_y/H as a function of the friction number S

It can be seen that there are relationships between the characteristic lengths and the friction number S which are given by the following equations:

$$\frac{\Lambda_x}{H} = 147 \times S + 2.8 \ (R^2 = 0.87) \tag{34}$$

$$\frac{\Lambda_y}{H} = 21 \times S^{0.44} \ (R^2 = 0.58) \tag{35}$$

However, dispersion of the points in Figure 22 is important. Two curves can be plotted (Figure 23): the dashed red curve corresponds to the regression of data collected by Peltier et al. (2014a,b,c) while the continuous red curve is obtained with present data.

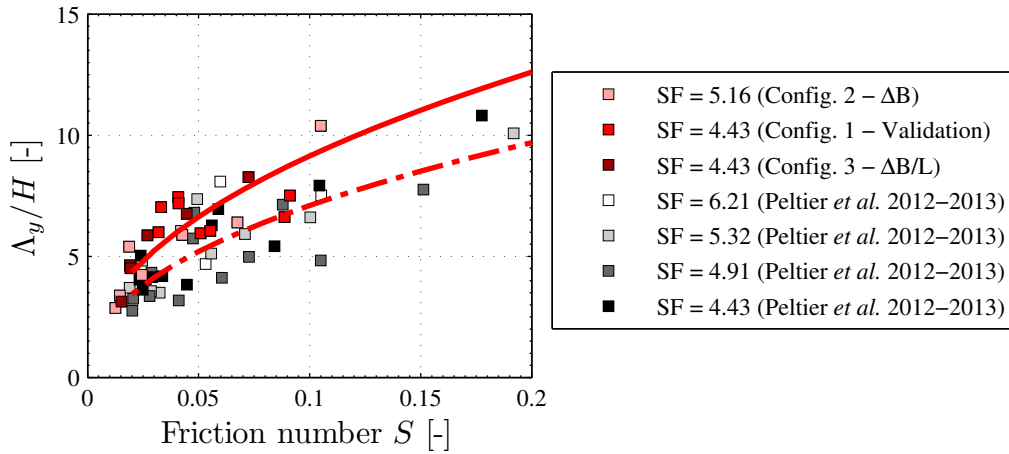FIGURE 23 – Evolution of the normalized characteristic length Λ_y/H as a function of the friction number S - Two regressions

The difference may result from the fact that the velocity fields determined by Peltier et al. (2014a,b,c) were not corrected in contrast to those obtained with present data.

In Figures 21 and 22, it can be seen that the correlation between the normalized characteristic lengths and the friction number is independent of the Shape Factor SF. Therefore, the water depth has more impact than the two other dimensions ΔB and L. Indeed, if we consider, for example, the two points in Figure 21 having a friction number of $0.17 - 0.19$, the corresponding normalized longitudinal characteristic length Λ_x/H is lower than 30 and the water depth H equals 0.012m which means that:

$$\frac{\Lambda_x}{H} < 30 \quad \& \quad H = 0.012m \tag{36}$$

$$\Rightarrow \Lambda_x < 30 \times H = 0.36m \tag{37}$$

Thus, Λ_x is smaller than the minimum experienced reservoir length which is equal to 0.7 m.

The same conclusion can be drawn regarding the lateral characteristic length Λ_y as it is equal to :

$$\frac{\Lambda_y}{H} < 15 \quad \& \quad H = 0.012m \tag{38}$$

$$\Rightarrow \Lambda_y < 15 \times H = 0.18m < B = 0.78m \tag{39}$$

In Figure 24, the ratio of the characteristic lengths Λ_x/Λ_y is represented with respect to the friction number S.
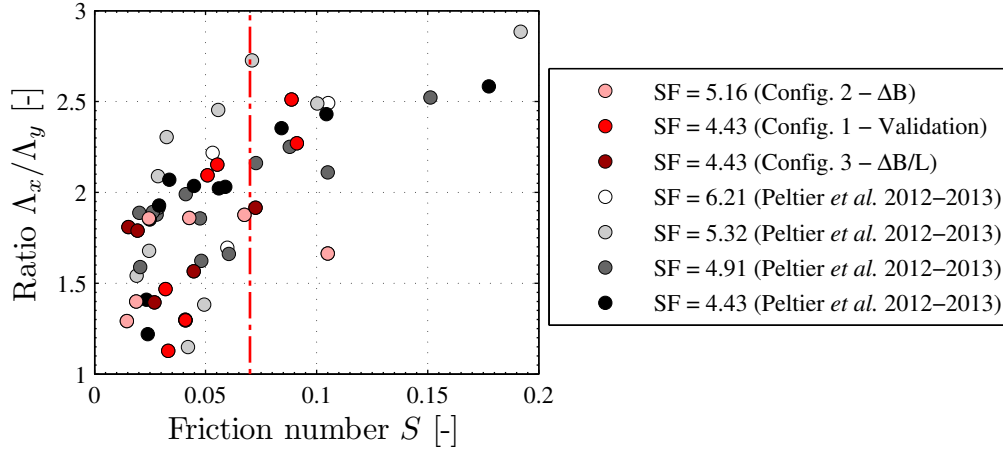
FIGURE 24 – Ratio of the characteristic lengths Λ_x/Λ_y represented with respect to the friction number S

As it was demonstrated in the validation phase, there is no relationship between the ratio Λ_x/Λ_y and the friction number when $S < 0.07$ corresponding to the non-frictional zone. For $S > 0.07$, the correlation that exists between these two factors is given by :

$$\frac{\Lambda_x}{\Lambda_y} = 8.1 \times S + 1.5 \ (R^2 = 0.60) \tag{40}$$

Moreover, no influence of the geometric parameters (width and length) can be found.

3.5.3.3 Strouhal number

The evolution of the Strouhal number St as a function of the friction number S is shown in Figure 25.
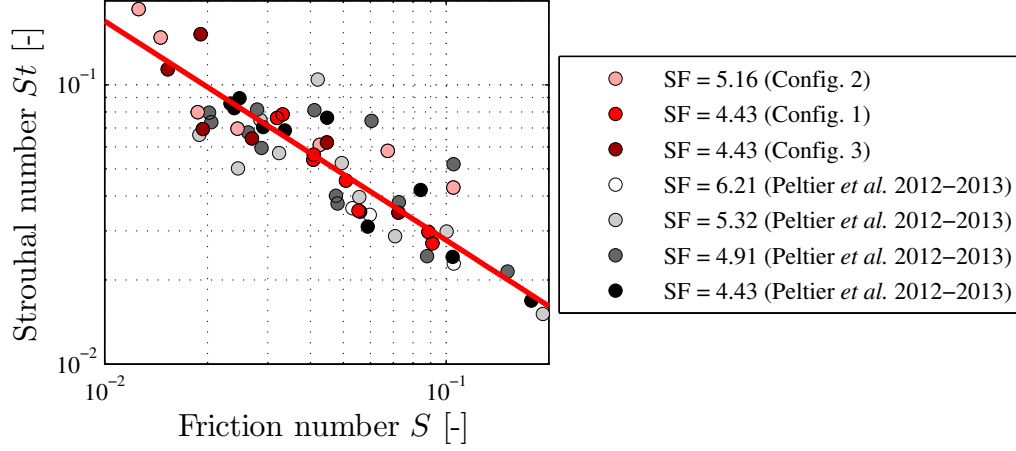
FIGURE 25 – Strouhal number St plotted with respect to the friction number S

The set of present data confirms the previously observed relationship between the Strouhal number St and the friction number S. The correlation writes :

$$St = 0.005 \times S^{-0.785} \ (R^2 = 0.75) \tag{41}$$

As in previous graphs, the width and the length of the reservoir do not seem to impact the relationship between the Strouhal number St and the friction number S.

3.5.4 POD analysis

The POD analysis was performed on 1000 snapshots in order to determine the eigenvalues λ_m.

We will now compare the temporal and spatial modes of the two configurations with the same Shape Factor SF (validation configuration and configuration with the width and the length that were modified). To do this, the results obtained for two discharges (0.25 L/s and 0.5 L/s) will be used (Tables 5 and 6).

3.5.4.1 Temporal coefficients

The temporal coefficients obtained for the five first modes for discharges of 0.25 L/s and 0.5 L/s are respectively displayed in Figures 26 and 27.

FIGURE 26 – Representation of the temporal coefficients of the five first mode corresponding to $Q = 0.25$ L/s for configurations 1 (left) and 3 ($\Delta B/L$) (right) - The *solid lines* represent odd modes and the *dotted lines* even modes

33

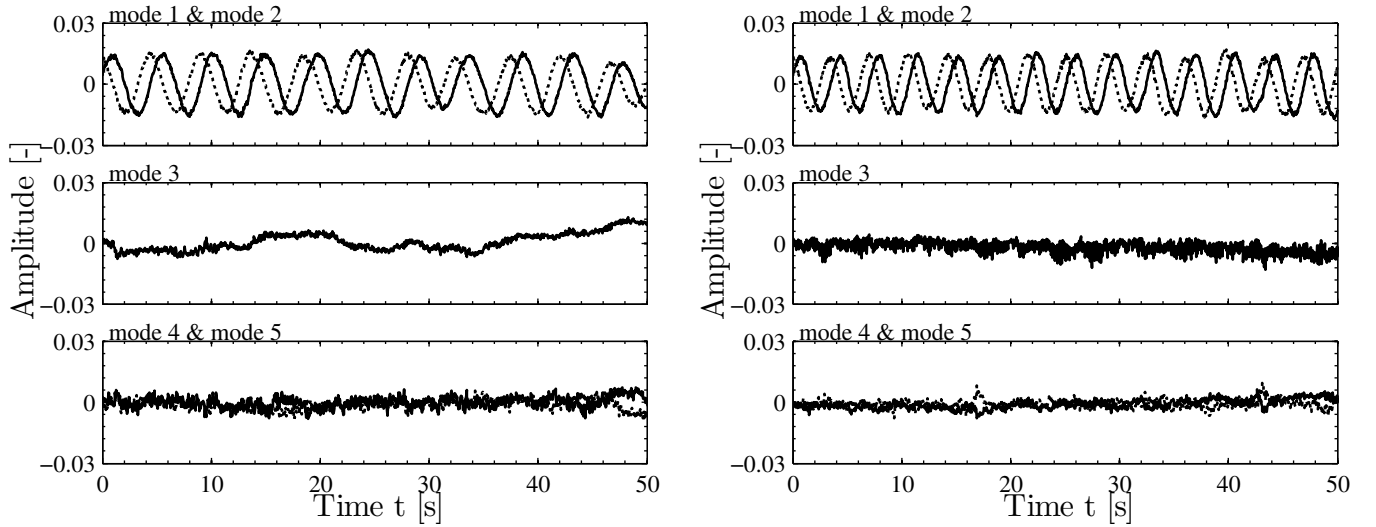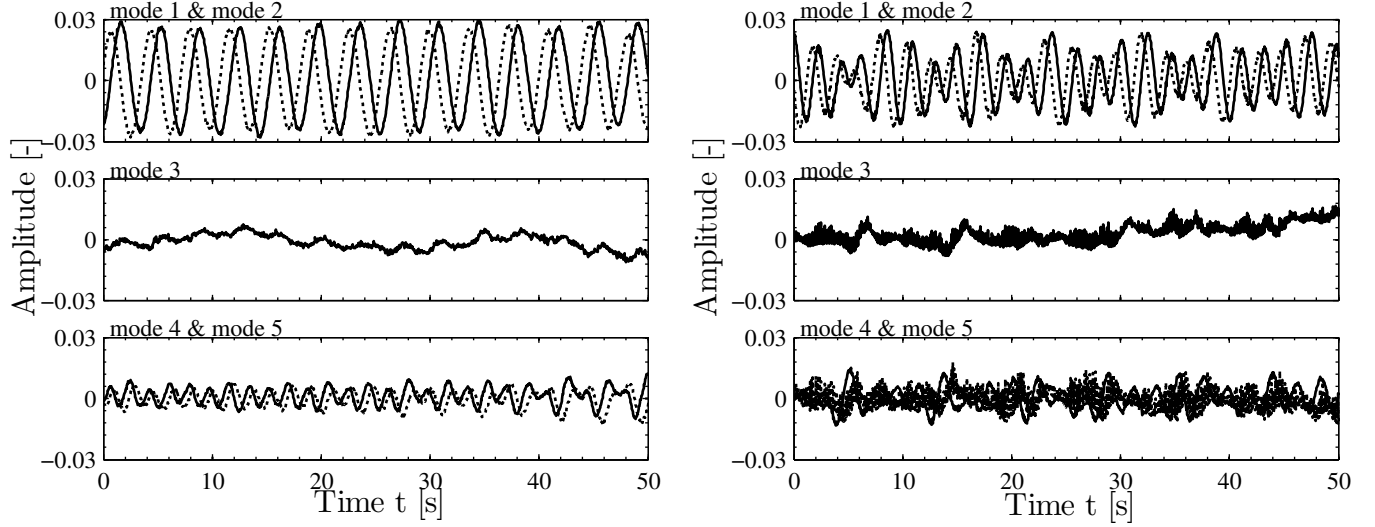FIGURE 27 – Representation of the temporal coefficients of the five first mode corresponding to $Q = 0.50$ L/s for configurations 1 (left) and 3 ($\Delta B/L$) (right) - The *solid lines* represent odd modes and the *dotted lines* even modes

For the smallest discharge, oscillations are regular for each configuration. The amplitude is almost identical ($A = 0.0157$ for the first configuration and $A = 0.155$ for the third one ($\Delta B/L$)) while the period is lower in third configuration.

For a discharge of 0.50 L/s, observed behavior in terms of regularity and amplitude are quite different from one configuration to another.

These differences do not only come from the geometry but also from the hydraulics parameters such as the Froude number and the friction number. However, it is not possible to make a comparison between the two configurations that include the same three parameters because we have too few experimental results.

3.5.4.2 Spatial modes

The spatial modes are also analyzed and for that, they are represented in Figure 28 and 29 for the first and the third configuration ($\Delta B/L$).

The first two modes have almost the same coherent structures that develop in the reservoir.

FIGURE 28 – Representation of the first five spatial modes for Q equals to 0.25 L/s for the first configuration - The *black rectangle* corresponds to a blank zone during the measurement - When the vorticity is negative, it is represented in blue while it is in red when it is positive

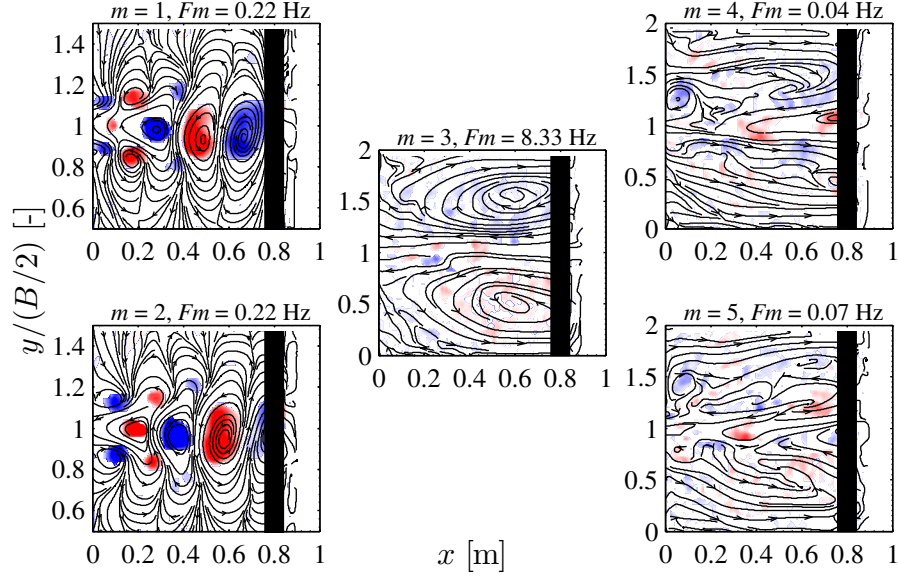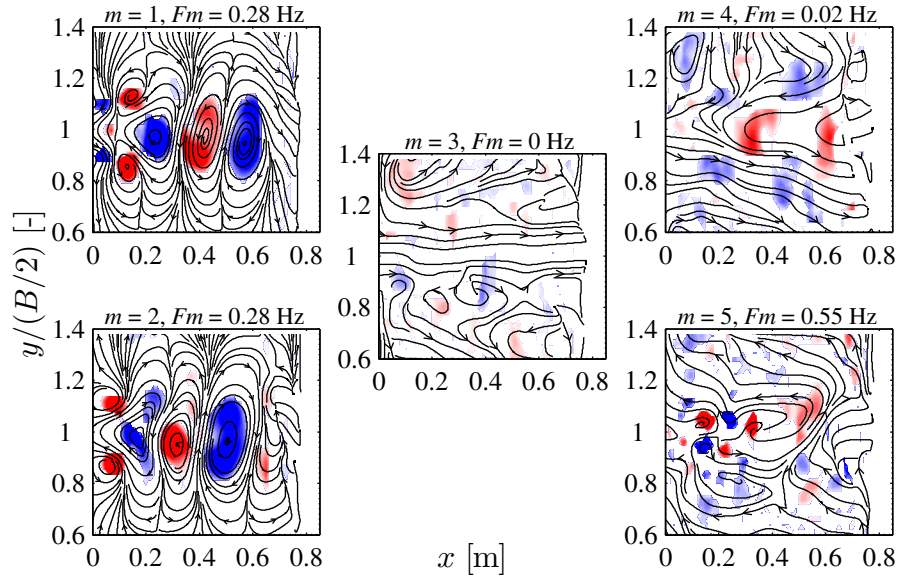FIGURE 29 – Representation of the first five spatial modes for Q equals to 0.25 L/s for the third configuration - The *black rectangle* corresponds to a blank zone during the measurement

3.5.5 Conclusion

In this subsection, three geometric configurations were analyzed. The first configuration is the one that was used to validate the experimental protocol in the previous subsection. In the second configuration, the reservoir width was changed but the length kept, which leads to a different Shape Factor between the first two configurations. In the last configuration, the width and the length of the reservoir were chosen so that the width is the same as the one of the second configuration and the length induced the same Shape Factor as the one of the first configuration.

At first, the domain of existence was studied and it was clearly shown that the boundaries between the different flow regimes are not yet well defined and so, this point needs to be improved in the future.

The normalized characteristic lengths and the Strouhal number were then compared to the Froude number and the friction number in order to determine the influence of the width or the length of the reservoir. Based on all the observations, it was possible to say that for a given flow regime (which depends on the Froude number and the Shape Factor), the geometrical parameters such as the length or the width of the reservoir do not influence the flow characteristics. These ones only depend on the friction number and so on the shallowness of the reservoir.

3.6 Conclusion

Throughout this first part devoted to experimental, the meandering flows were studied and the impact of geometrical parameters on their characteristics was studied.

In order to validate the experimental protocol, a first configuration was studied and the results obtained were compared with those of Peltier et al. (2014a,b,c). Then, two other configurations were used to analyzed the influence of the resevoir geometry on properties of meandering flows.

This second part has shown that for a given flow regime, the characteristics of the flow does not depend on the geometry but on the friction number that represents the shallowness of the reservoir.

A study of the domain of existence was also performed and it was shown that the boundaries between the different flow regimes were not yell defined so far and that they need to be analyzed in more detail in the future.

4 Can thermodynamic principles help to predict the flow pattern in the reservoir ?

4.1 Introduction

Prediction of deposit patterns in reservoirs is a critical issue for their optimal design, sizing, operation and maintenance and depends on the knowledge of flow patterns. Over the last years, reservoir hydrodynamics and sedimentation patterns have been studied experimentally and numerically. Thus, a large set of data was collected through experimental research (Dufresne et al. (2012); Kantoush et al. (2008)) and numerical models were used to predict the flow fields.

However, experimental research has limits and numerical models are generally computationally intensive, data demanding and relatively complex to set up. Moreover, they deliver a large amount of results, from which it is difficult to extract the governing phenomena.

This section will be devoted to the development of a simple analytical model which will allow to improve understanding of fluid mechanics processes. The study will focuses on the applicability of the principle of maximum power (see state of the art) to determine if the flow is symmetric or asymmetric (Dufresne et al. (2012) and Peltier et al. (2014a,b,c) showed that this flow regime transition appears for a Shape Factor varying between $6.2 - 8.1$)

To do that, two models will be developed : one symmetric and the other asymmetric. In each of these models, mass balance and momentum balance equations will be established and will be used to determine velocities or the pressure gradient. After being determined, the powers of the two models will be plotted as a function of the Shape Factor in order to see if the principle of maximum power can be used.

4.2 Conceptual model

In this conceptual approach, the complex flow in the reservoir is idealized by three simple structures: a main jet and two vortices present on both sides of the jet. The geometric parameters such as the length or the width of the reservoir or the width of inlet and outlet are considered as input data. The inflow discharge and the water depth which is controlled from the downstream boundary are also part of the known data.

Mass balance is used to determine the flow velocity in the main jet based on geometrical parameters of the jet and the inflow discharge. Then, momentum balance is applied to each flow component, which allows to obtain the recirculation velocities and the pressure gradient.

At first, the flow is assumed to be straight and the flow field is considered symmetric with respect to the centerline of the reservoir. This configuration is defined as the *reference solution*.
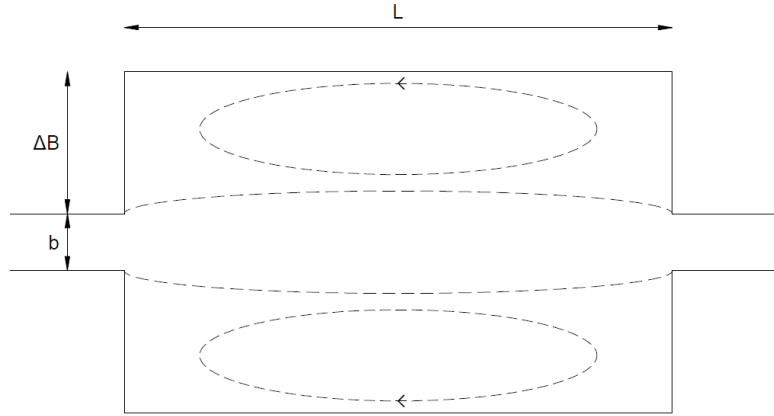

FIGURE 30 – Reference configuration considering a straight jet

In a second step, an asymmetrical flow is considered as the *perturbed solution*. In this case, the flow is attached to a side wall of the reservoir.
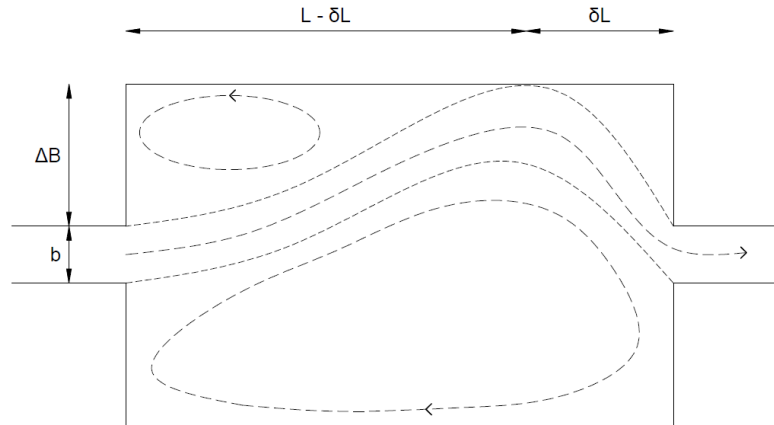

FIGURE 31 – Perturbed configuration with jet reattachment

4.3   Numerical modelling

In order to check the values obtained from the mathematical model, the results of simulations carried out by Camnasio et al. (2014) were exploited.

4.3.1   WOLF 2D

Numerical modeling was performed with the numerical model WOLF 2D developed at the University of Liege. This model is based on the shallow-water equations which assume that the flow is mainly two-dimensional and solves them using a finite volume scheme. Considering a flat bottom, the equations of mass and momentum conservation write : [Camnasio et al. (2014); Dewals et al. (2008)]

$$\frac{\partial h}{\partial t} + \frac{\partial hu}{\partial x} + \frac{\partial hv}{\partial y} = 0 \tag{42}$$

$$\frac{\partial hu}{\partial t} + \frac{\partial hu^2}{\partial x} + \frac{\partial huv}{\partial y} + \frac{\partial}{\partial x}\left(\frac{gh^2}{2}\right) = \frac{\tau_{bx}}{\rho} + \frac{1}{\rho}\frac{\partial h\sigma_x}{\partial x} + \frac{1}{\rho}\frac{\partial h\tau_{xy}}{\partial y} \tag{43}$$

$$\frac{\partial hv}{\partial t} + \frac{\partial huv}{\partial x} + \frac{\partial hv^2}{\partial y} + \frac{\partial}{\partial y}\left(\frac{gh^2}{2}\right) = \frac{\tau_{by}}{\rho} + \frac{1}{\rho}\frac{\partial h\tau_{xy}}{\partial x} + \frac{1}{\rho}\frac{\partial h\sigma_y}{\partial y} \tag{44}$$

Variable reconstruction is performed linearly at cells interfaces, combined with a slope limiter. This type of reconstruction leads to a second-order spatial accuracy. The convective fluxes are computed by a Flux Vector Splitting (FVS). This method offers the advantage of being robust and Froude-independent. The time integration is performed by means of a 3-step Runge-Kutta algorithm. A Courant-Friedrichs-Levy (CFL) condition is used to constrain the time step for stability reasons [Dewals et al. (2008); Peltier et al. (2015)].

A two length-scale depth-averaged turbulence model is used to evaluate the turbulent fluxes. The bed-generated turbulence is given by :

$$\nu_{T,3D} = 0.08hu^* \tag{45}$$

where u^* is the friction velocity.

The horizontal mixing, associated to the large-scale transverse shear-generated turbulence is modeled by $\nu_{T,2D} = c_\mu \frac{k^2}{\varepsilon}$. The variables k and ε are determined by two transport equations. [Camnasio et al. (2014); Peltier et al. (2015)]

4.3.2   Numerical data-set

Now that the functioning of the numerical model used is described, we will focus on the conditions and variables imposed by Camnasio et al. (2014).

In all simulations, a constant water surface elevation of 0.2 m was considered as the outflow boundary condition. At the inlet, a constant unit discharge $hu = 0.028m^2/s$ was set as the downstream boundary condition, which results in a total discharge Q of 7 L/s. A slight transverse disturbance of about 1% was applied in the inflow profile of unit discharge in order to test the stability of the flow field. However, Camnasio et al. (2014) showed that this disturbance had any effect on the flow pattern, except in the transition zone (i.e. $SF \sim 6.8$). In our case, only flows outside of this transition zone interest us and so, this disturbance will not have any impact on the results.

In her numerical models, Camnasio et al. (2014) used a grid of $2.5cm \times 2.5cm$ and the time step is of the order of 5×10^{-3} seconds, as it depends on the Courant-Friedrichs-Lewy stability condition.

At solid walls, the shear velocity is evaluated using the law of the wall and the depth-integrated turbulent kinetic energy and the dissipation rate are determined using the following equations developed by Erpicum et al. (2009) :

$$k' = \frac{hU_\tau^2}{\sqrt{c_\mu}} \quad \text{and} \quad \varepsilon = \frac{h^2 U_\tau^3}{\kappa d} \tag{46}$$

where U_τ corresponds to the shear velocity assuming a logarithmic velocity profile near the wall, κ is the von Karman constant and d is the distance from the wall.

At the inlets, these two variables are calculated based on the paper of Choi and Garcia (2002) :

$$k' = 10^{-4}hu^2 \quad \text{and} \quad \varepsilon = 10\frac{k^{3/2}}{\sqrt{h}} \tag{47}$$

4.3.3 Numerical results

In her paper, Camnasio et al. (2014) compares the numerical results of the cross-sectional profiles of the longitudinal velocity with those obtained experimentally (Figure 32) and showed that they are almost identical. We can therefore used these simulations to verify the results obtained with the mathematical model.
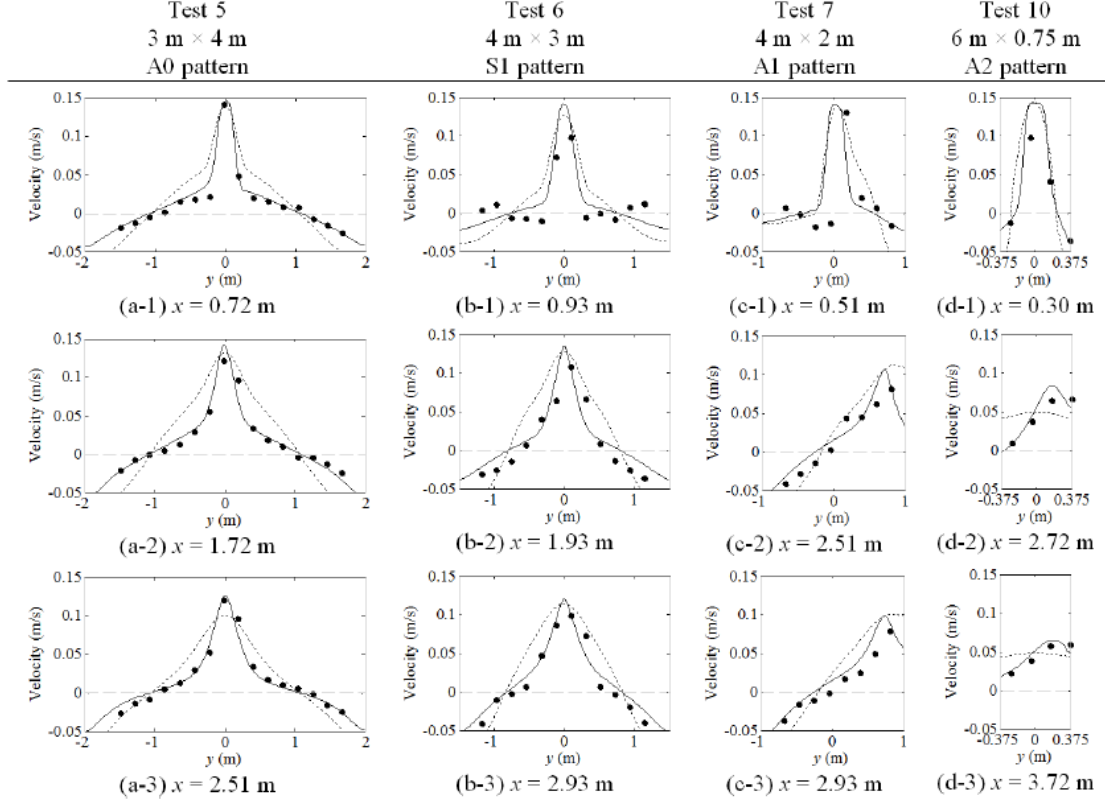
FIGURE 32 – Observed and computed cross-sectional velocity profiles for the four reservoir geometries corresponding to tests 5,6,7 and 10 : experimental ($\bullet$) and simulated with the $k - \varepsilon$ model (—) and with the algebraic turbulence model ($--$) - [Camnasio et al. (2014)]

In Table 7, geometric data of several configurations related to symmetric flows are listed. The recirculation discharge Q_r is also determined. In Figure 33, it corresponds to the total discharge passing through the section represented by a black line.
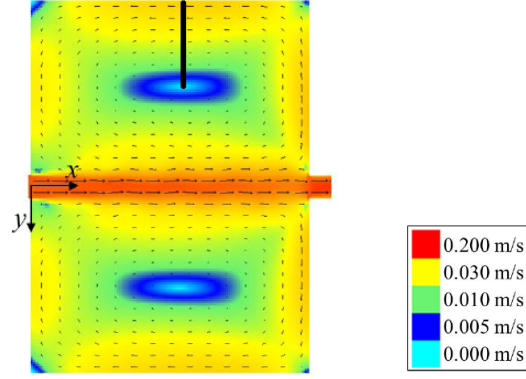
FIGURE 33 – Flow field obtained using the depth-averaged $k - \varepsilon$ model (Test 5). The *black line* corresponds to the section where the recirculation discharge is evaluated - [Camnasio et al. (2014)]

Length L $[m]$	Width B $[m]$	Shape factor SF $[-]$	Discharge Q_r $[m^3/s]$
4.5	4	5.4	0.0051
5.3	4	6.3	0.0050
5.5	4	6.6	0.0050

TABLE 7 – Data corresponding to symmetric flow

4.4 Symmetric model N°1

In order to simplify this first model, only one lateral expansion in the reservoir is considered. In addition, the separation between the recirculation zone and the principal jet is idealized by a straight line.
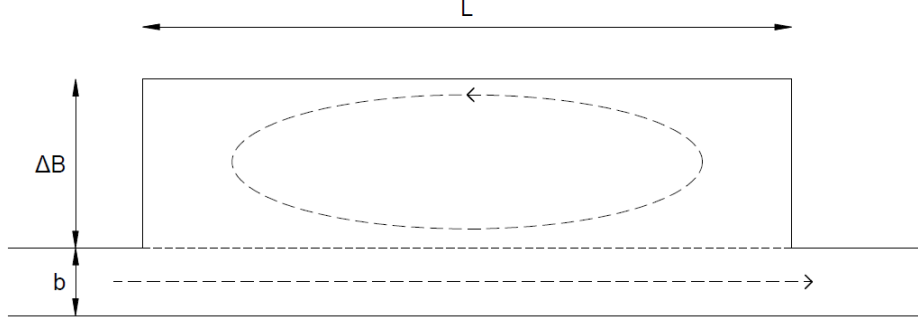
FIGURE 34 – Simplified reference configuration considering a straight jet

4.4.1 General approach

In this general approach, we assume that all geometric effects are lumped into extended resistance coefficients C_b and C_s. Based on this assumption, the momentum equation for the recirculation flow writes:

$$C_b u_L^2 = C_s \left(u - u_L\right)^2 \tag{48}$$

where u is the jet velocity and u_L is the velocity of the recirculating cavity flow at the interface with the jet.

After some developments (see Appendix B.1.1), this expression can be written in the following non-dimensional form:

$$\frac{u_L}{u} = \frac{-\frac{C_s}{C_b} \pm \sqrt{\frac{C_s}{C_b}}}{1 - \frac{C_s}{C_b}} \tag{49}$$

At the interface between the jet and the recirculation cavity flow, the power of the shear force is given by:

$$P = C_s \left(u - u_L\right)^2 \left(u - u_L\right) \tag{50}$$
$$= C_s \left(u - u_L\right)^3 \tag{51}$$

In non-dimensional form, it writes: (See Appendix B.1.2)

$$\tilde{P} = \frac{P}{C_b u^3} \tag{52}$$
$$= \gamma \left(\frac{1 \mp \sqrt{\gamma}}{1 - \gamma}\right)^3 \tag{53}$$

44

where $\gamma = \frac{C_s}{C_b}$.

Only one of these two solutions leads to a distinct maximum in the power, as shown in the graph below plotting the non-dimensional power as a function of the parameter γ.
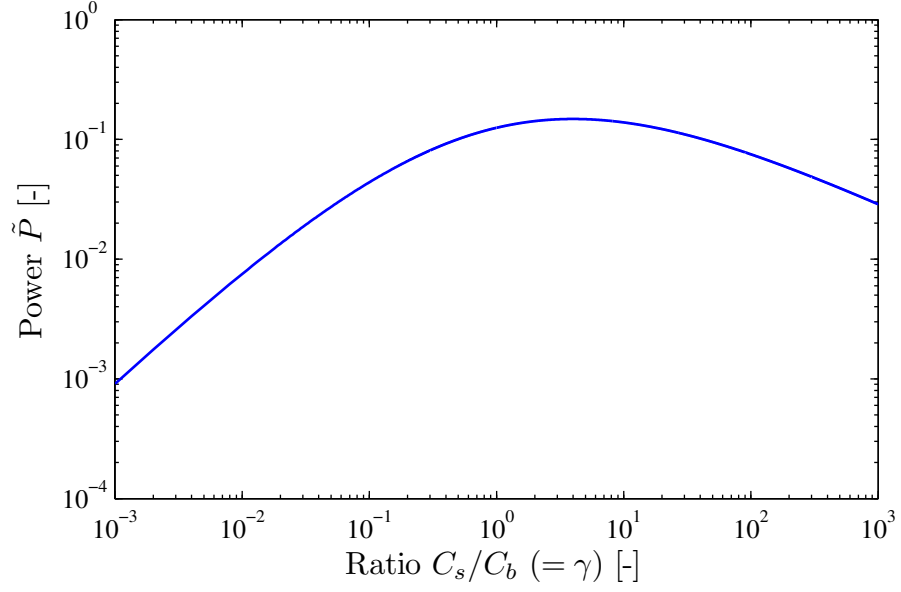
FIGURE 35 – Evolution of power according to the parameter γ

This peak corresponds to a ratio C_s/C_b equals to 4 and a velocity ratio u_L/u of 0.6667.

4.4.2 Reference solution - Model description
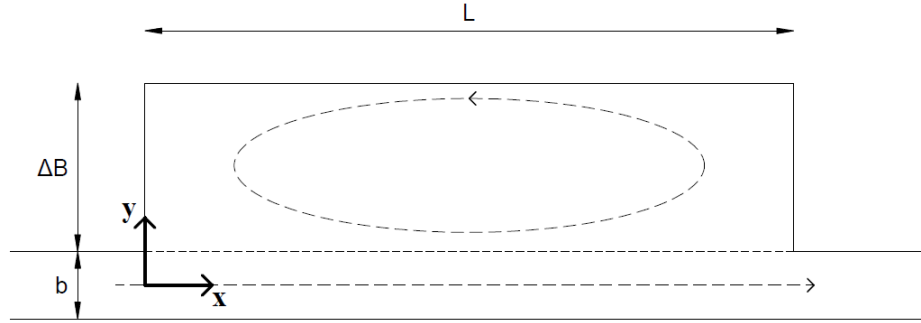
FIGURE 36 – Mathematical model 1 : Reference configuration

In this first configuration, the velocity along x-axis is distributed parabolically. Thus, the velocity in $L/2$ is maximum and decreases at the extremities. The velocity along y-axis is also parabolic but reaches its maximum at $\Delta B/2$. The velocities also decrease as they approach the center of recirculation. A schematic representation of the velocity fields is shown in Figure 37.
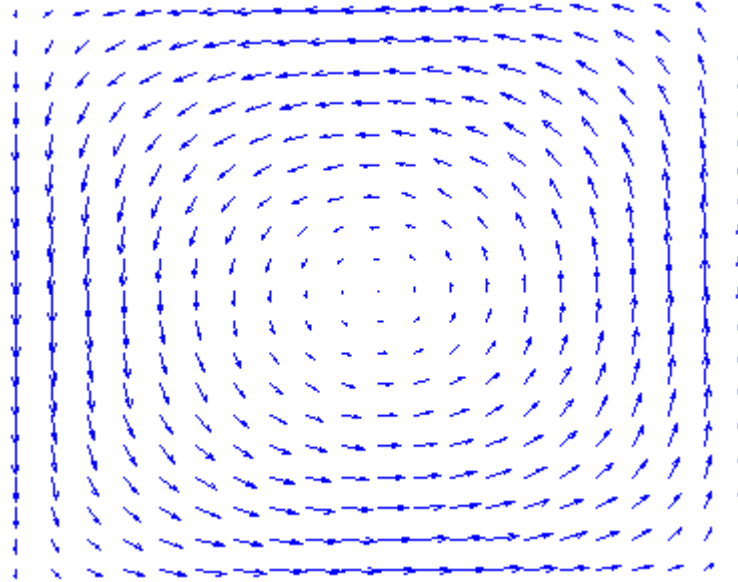
FIGURE 37 – Representation of the velocity fields

4.4.3   Distribution of velocities

Considering the following conditions:

$$
\begin{aligned}
x &= L/2 \,; y = b/2 & &\Rightarrow u_\omega = V_0 \\
x &= L/2 \,; y = b/2 + \Delta B & &\Rightarrow u_\omega = -V_0 \\
x &= 0 \quad ; y = b/2 + \Delta B/2 & &\Rightarrow u_\omega = 0 \\
x &= L \quad ; y = b/2 + \Delta B/2 & &\Rightarrow u_\omega = 0
\end{aligned}
$$

The velocity along x varies linearly between 0 at the center of the lateral expansion and V_0 at the interface between the straight jet and the recirculation zone. It can be written:

$$
u_\omega = -V_0 \frac{2}{\Delta B} \left(y - \frac{b + \Delta B}{2} \right) (x - L)\, x \left(\frac{-4}{L^2} \right) \tag{54}
$$

The same thing can be done to obtain the expression of the velocity along y. We have:

$$
\begin{aligned}
x &= L/2 \,; y = b/2 & &\Rightarrow v_\omega = 0 \\
x &= L/2 \,; y = b/2 + \Delta B & &\Rightarrow v_\omega = 0 \\
x &= 0 \quad ; y = b/2 + \Delta B/2 & &\Rightarrow v_\omega = -\tilde{V_0} \\
x &= L \quad ; y = b/2 + \Delta B/2 & &\Rightarrow v_\omega = \tilde{V_0}
\end{aligned}
$$

$$
v_\omega = -\tilde{V_0} \left(\frac{-4}{\Delta B^2} \right) \left(y - \frac{b}{2} \right) \left(y - \frac{b}{2} - \Delta B \right) \left(x - \frac{L}{2} \right) \left(\frac{-2}{L} \right) \tag{55}
$$

with, (see Appendix B.1.3)

$$
\tilde{V_0} = \frac{\Delta B}{L} V_0 \tag{56}
$$

In non-dimensional forms, these two equations write:

$$
\frac{u_\omega}{V_0} = 4 \left(\frac{b}{\Delta B} + 1 - \frac{2y}{\Delta B} \right) \left(1 - \frac{x}{L} \right) \frac{x}{L} \tag{57}
$$

$$
\frac{v_\omega}{V_0} = 4 \frac{\Delta B}{L} \left(\frac{b}{2\Delta B} - \frac{y}{\Delta B} \right) \left(\frac{y}{\Delta B} - \frac{b}{2\Delta B} - 1 \right) \left(\frac{2x}{L} - 1 \right) \tag{58}
$$

4.4.4   Mass and momentum balance equations

The mass balance equation write:

$$Q = u_0 bh \tag{59}$$

where Q = discharge, u_0 = velocity in the straight jet, b = inlet width, h = water depth.

Based on the velocity equations, the momentum balance equation in the straight jet can be expressed as:

$$\frac{\Delta p_0}{\rho} hb = c_b u_0^2 bL + \underbrace{\int_0^L c_s \left[u_0 - u_\omega \left(x, \frac{b}{2} \right) \right]^2 hdx}_{\text{(see Appendix B.1.4)}} \tag{60}$$

$$\frac{\Delta p_0}{\rho} hb = c_b u_0^2 bL + c_s hL \left(u_0^2 - \frac{4}{3} u_0 V_0 + \frac{8}{15} V_0^2 \right) \tag{61}$$

with ρ the water density, c_s the shear coefficient between the straight jet and the recirculation zone and c_b the friction coefficient on the bottom.

In equation (61), the first term is a pressure difference which is equal to, on one hand, a loss due to bottom friction and, on the other hand, a loss by shear friction between the straight jet and the recirculation zone.

The momentum balance in the recirculation is given by:

$$\underbrace{\int_S c_b \omega^2(x, y) dS}_{\text{(see Appendix B.1.5)}} = \underbrace{\int_0^L c_s \left[u_0 - u_\omega \left(x, \frac{b}{2} \right) \right]^2 hdx}_{\text{(see Appendix B.1.4)}} \tag{62}$$

$$\frac{8}{45} c_b V_0^2 \Delta BL \left(\frac{\Delta B^2}{L^2} + 1 \right) = c_s hL \left(u_0^2 - \frac{4}{3} u_0 V_0 + \frac{8}{15} V_0^2 \right) \tag{63}$$

$$\frac{8}{45} c_b V_0^2 \Delta B \left(\frac{\Delta B^2}{L^2} + 1 \right) = c_s h \left(u_0^2 - \frac{4}{3} u_0 V_0 + \frac{8}{15} V_0^2 \right) \tag{64}$$

where $\omega(x, y)$ represents the resulting velocity in the recirculation zone.

Based on this equation, we can proceed in the same way as for the generalized approach, which allows to obtain the velocity ratio V_0/u_0. In non-dimensional form, it writes: (see Appendix B.1.6)

$$\frac{V_0}{u_0} = \frac{-\frac{1}{3} \frac{c_s}{c_b} \pm \sqrt{-\frac{1}{45} \left(\frac{c_s}{c_b} \right)^2 + \frac{2}{45} \frac{c_s}{c_b} \frac{\Delta B}{b} \frac{b}{h} \left(\left(\frac{\Delta B}{L} \right)^2 + 1 \right)}}{4 \left[\frac{1}{45} \frac{\Delta B}{b} \frac{b}{h} \left(\left(\frac{\Delta B}{L} \right)^2 + 1 \right) - \frac{1}{15} \frac{c_s}{c_b} \right]} \tag{65}$$

48

At the interface between the jet and the recirculation cavity flow, the power shear force is given by:

$$P = h \int_0^L c_s \left(u_0 - u_\omega \left(x, b/2 \right) \right)^2 \left(u_0 - u_\omega \left(x, b/2 \right) \right) dx \tag{66}$$

$$= h \int_0^L c_s \left(u_0 - u_\omega \left(x, b/2 \right) \right)^3 dx \tag{67}$$

In non-dimensional form, it writes: (see Appendix B.1.7)

$$\tilde{P} = \frac{P}{c_b u_0^3 h L} \tag{68}$$

$$= \frac{c_s}{c_b} \int_0^1 \left(1 - \frac{u_\omega \left(\beta, b/2 \right)}{V_0} \frac{V_0}{u_0} \right)^3 d\beta \tag{69}$$

$$= \frac{c_s}{c_b} \left[-\frac{16}{35} \left(\frac{V_0}{u_0} \right)^3 + \frac{8}{5} \left(\frac{V_0}{u_0} \right)^2 - 2 \left(\frac{V_0}{u_0} \right) + 1 \right] \tag{70}$$

4.4.5 Results and discussion

For example, in order to represent the results, a configuration in which the length L is equal to 4 m, the inlet width b to 0.08m and the width B to 2m ($SF = 5.8$) is used.

The velocity ratio V_0/u_0 is plotted against c_s/c_b in Figure 38. Only the positive solution of equation (65) is represented, the negative one having no physical meaning. Moreover, only real numbers are plotted in this graph. Indeed, the domain of the function is limited by the following condition:

$$\sqrt{ -\frac{1}{45} \left(\frac{c_s}{c_b} \right)^2 + \frac{2}{45} \frac{c_s}{c_b} \frac{\Delta B}{b} \frac{b}{h} \left(\left(\frac{\Delta B}{L} \right)^2 + 1 \right) } > 0 \tag{71}$$

$$\Rightarrow \frac{c_s}{c_b} < 2 \frac{\Delta B}{b} \frac{b}{h} \left(\left(\frac{\Delta B}{L} \right)^2 + 1 \right) \tag{72}$$

$$\Rightarrow \frac{c_s}{c_b} < 15.37 \tag{73}$$

The higher the ratio, the more the velocity ratio increases. This is due to the greater exchange between the straight jet and the recirculation zone, which leads to an equalization of the two velocities. However, for c_s/c_b above 6.76, the velocity ratio is greater than unity, which is not physical.

49
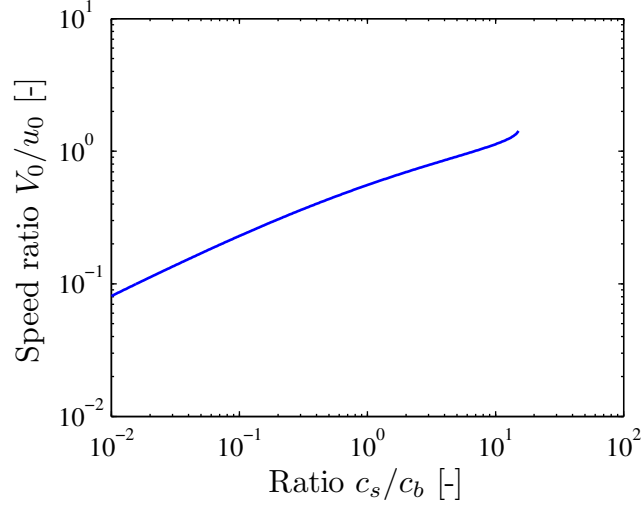
FIGURE 38 – Velocity ratio V_0/u_0 plotted with respect to the ratio c_s/c_b

In Figure 39, the evolution of the non-dimensional power $\tilde{P}$ as a function of the ratio c_s/c_b is shown. This curve increases until it reaches a peak for c_s/c_b equals to 13.18. However, only the values on the left of the dashed vertical line are in the physical domain. Thus, the power is reduced to an increasing curve, which differs from the result obtained in the general approach.

FIGURE 39 – Non-dimensional power shear force $\tilde{P}$ plotted against the ratio c_s/c_b

4.4.6 Conclusion

This first simplified model studies the equations of mass and momentum conservation in the case of a symmetric flow.

Based on the equation of momentum in the recirculation, the ratio between the maximum velocity in the recirculation and the velocity in the straight jet was obtained and the power of the shear force was then evaluated.

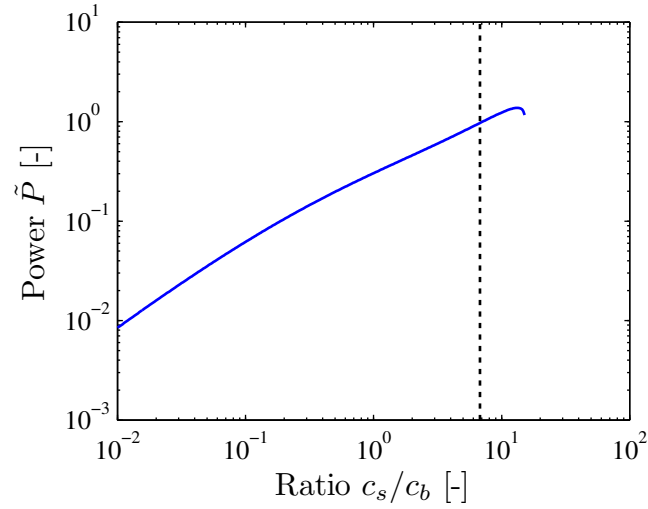The velocity ratio and the non-dimensional power were plotted against the ratio c_s/c_b, leading in both cases to a rising curve only if the physical domain is considered. This result is not appropriate because it does no provide a maximum in the power curve as it was the case in the generalized approach.

Moreover, the distribution of the velocity u_ω along the straight jet is always parabolic (along the x-axis), and that, for all values of c_s. Thus, if c_s tends to infinity, the velocity u_ω along the interface does not, at any points, tends to the velocity in the straight jet u_0.

In conclusion, this model does not allow to reproduce the physical phenomena occurring. The assumptions made about the distribution of the velocity u_ω must be reconsidered.

4.5 Symmetric model N°2

4.5.1 Model description

In order to fix the problem raised by the previous model, the flow field in the recirculation cell is now schematized differently. The cavity is divided into four parts (Figure 40). Velocities in each triangle are unidirectional and decrease linearly as they approach the center (intersection of the two diagonals). Thus, in triangles 1 and 3, only the velocity along the x-axis is non-zero. On the contrary, in triangles 2 and 4, only the velocity along the y-axis is non-zero.
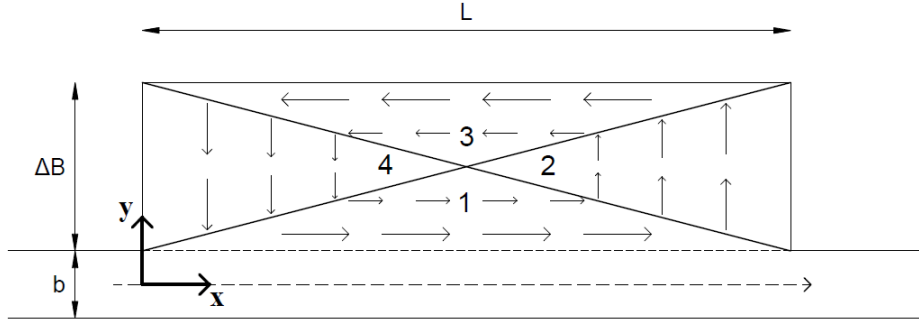
FIGURE 40 – Mathematical model 2 : Reference configuration

4.5.2 Distribution of velocities

In triangle 1, we have the following conditions:

$$y = b/2 \qquad \Rightarrow u_1 = V_0$$
$$y = b/2 + \Delta B/2 \Rightarrow u_1 = 0$$

The corresponding velocities write:

$$u_1 = V_0 \left(\frac{b}{2} + \frac{\Delta B}{2} - y \right) \frac{2}{\Delta B} \; ; \; v_1 = 0 \tag{74}$$

The same thing can be done for the other three triangles. Thus for the triangle 2, we have:

$$x = L \quad \Rightarrow v_2 = \tilde{V}_0$$
$$x = L/2 \Rightarrow v_2 = 0$$

$$u_2 = 0 \; ; \; v_2 = \tilde{V}_0 \left(x - \frac{L}{2} \right) \frac{2}{L} \tag{75}$$

with, (see Appendix B.2.1)

$$\tilde{V}_0 = \frac{\Delta B}{L} V_0 \tag{76}$$

Regarding velocities in triangle 3 and 4, they are respectively identical to those for triangle 1 and 2.

In non-dimensional form, equations (74) and (75) write:

$$\frac{u_{1,3}}{V_0} = \left(\frac{b}{\Delta B} + 1 - \frac{2y}{\Delta B}\right) \tag{77}$$

$$\frac{v_{2,4}}{V_0} = \frac{\Delta B}{L}\left(\frac{2x}{L} - 1\right) \tag{78}$$

4.5.3 Mass and momentum balance equations

The mass balance equation in the straight jet can be written as:

$$Q = u_0 b h \tag{79}$$

The momentum balance equation in the straight jet writes:

$$\frac{\Delta p_0}{\rho} h b = c_b u_0^2 b L + \int_0^L c_s \left[u_0 - u_1\left(\frac{b}{2}\right)\right]^2 h dx \tag{80}$$

$$\frac{\Delta p_0}{\rho} h b = c_b u_0^2 b L + c_s \left(u_0 - V_0\right)^2 h L \tag{81}$$

In the recirculation zone, the momentum balance equation is given by:

$$\underbrace{c_b\left[\int_{S_1} v_1^2 dS_1 + \int_{S_2} v_2^2 dS_2 + \int_{S_3} v_3^2 dS_3 + \int_{S_4} v_4^2 dS_4\right]}_{\text{(see Appendix B.2.2)}} = \int_0^L c_s \left[u_0 - u_1\left(\frac{b}{2}\right)\right]^2 h dx \tag{82}$$

$$\frac{1}{4} c_b \Delta B L \left[\left(\frac{\Delta B}{L}\right)^2 + 1\right] V_0^2 = c_s h L \left[u_0 - u_1\left(\frac{b}{2}\right)\right]^2 \tag{83}$$

$$\frac{1}{4} c_b \Delta B \left[\left(\frac{\Delta B}{L}\right)^2 + 1\right] V_0^2 = c_s h \left[u_0 - u_1\left(\frac{b}{2}\right)\right]^2 \tag{84}$$

By developing this equation, the ratio between the two velocities V_0 and u_0 can be expressed as follows:

$$\frac{V_0}{u_0} = \frac{-\frac{c_s}{c_b} \pm \sqrt{\frac{1}{4}\frac{c_s}{c_b}\frac{\Delta B}{b}\frac{b}{h}\left(\left(\frac{\Delta B}{L}\right)^2 + 1\right)}}{\left[\frac{1}{4}\frac{\Delta B}{b}\frac{b}{h}\left(\left(\frac{\Delta B}{L}\right)^2 + 1\right) - \frac{c_s}{c_b}\right]} \tag{85}$$

The power developed by the shear force can be written as:

$$P = h \int_0^L c_s \left(u_0 - u_1\left(\frac{b}{2}\right)\right)^2 \left(u_0 - u_1\left(\frac{b}{2}\right)\right) dx \tag{86}$$

$$= h L \left(u_0 - V_0\right)^3 \tag{87}$$

53

The non-dimensional form writes:

$$\tilde{P} = \frac{P}{c_b h L u_0^3} \tag{88}$$

$$= \frac{c_s}{c_b} \left(1 - \frac{V_0}{u_0} \right)^3 \tag{89}$$

The flow in the recirculation is given by:

$$Q_r = \frac{1}{2} h \frac{\Delta B}{2} \frac{V_0}{u_0} u_0 \tag{90}$$

4.5.4 Results and discussion

In order to plot the results, the geometric parameters of the reservoir are chosen:

$$b = 0.25m$$
$$B = 3.00m$$

(91)

The non-dimensional power developed by the shear force is plotted with respect to the ratio c_s/c_b for various basin lengths in Figure 41. As in the previous model, only the physical solution is shown. The power $\tilde{P}$ reaches a maximum for values of ratio c_s/c_b varying between 5 and 15. This maximum decreases when the length L increases.
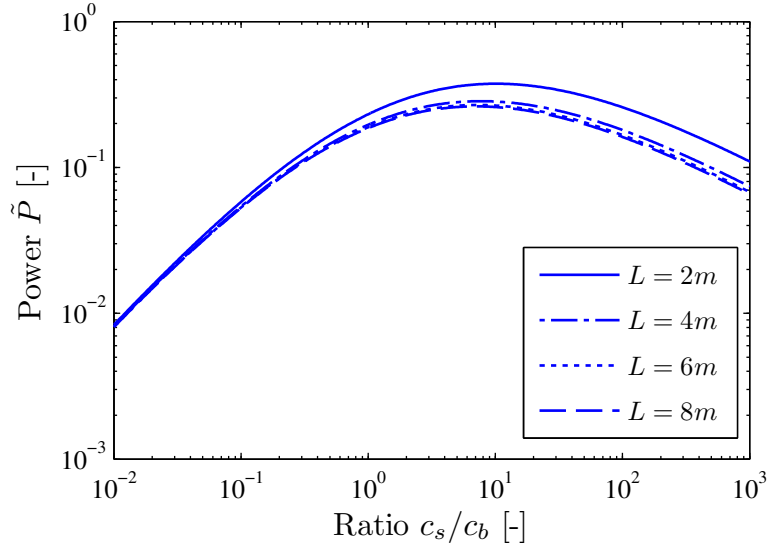

FIGURE 41 – Non-dimensional power $\tilde{P}$ plotted against the ratio c_s/c_b for different lengths L

The velocity ratio tends towards unity for increasing values of c_s/c_b (Figure 42). When the ratio c_s/c_b increases, the shear interaction between the jet and the recirculation zone is higher and the velocity V_0 in the recirculation zone tends to the velocity u_0.
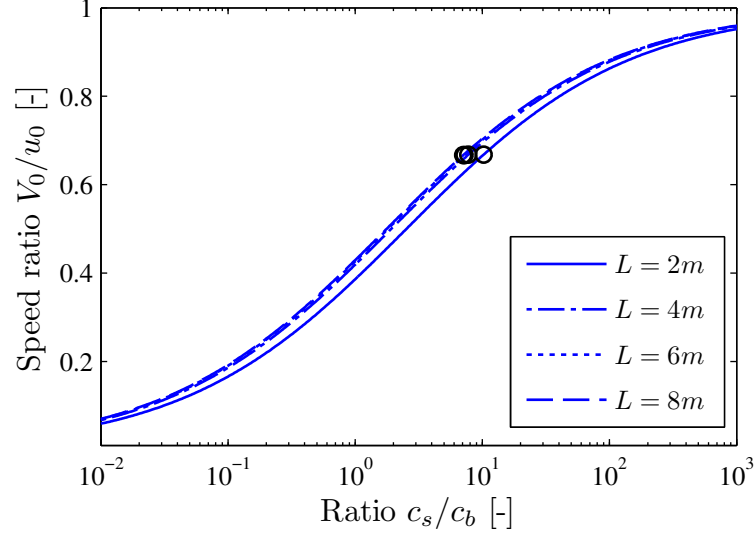
FIGURE 42 – Velocity ratio V_0/u_0 plotted with respect to the ratio c_s/c_b for various lengths L

The black circles corresponds to the velocity ratio at maximum power. The evolution depending on the length L is shown in Figure 43 and seems to be constant for a value of 0.6667.
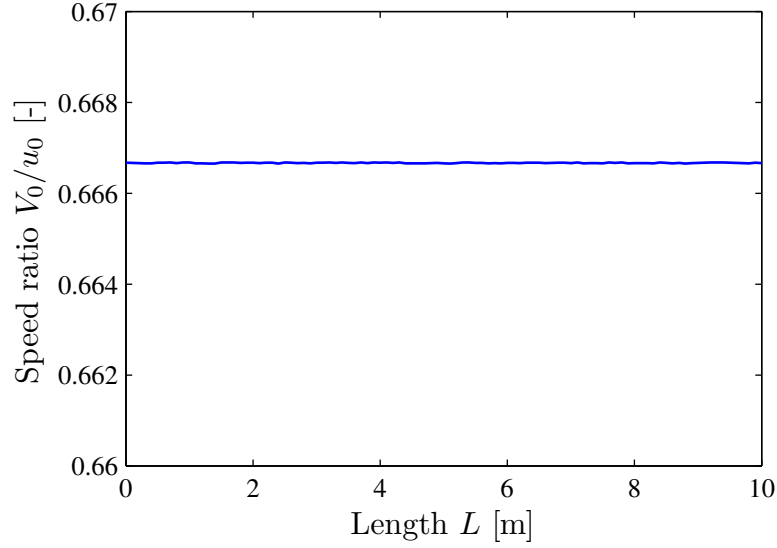
FIGURE 43 – Evolution of the velocity ratio V_0/u_0 (corresponding at maximum power) depending on the length L

The pressure gradient is plotted with respect to the ratio c_s/c_b for various reservoir lengths in Figure 44. In order to plot these graphs, the friction coefficient of the bottom was determined based on the Colebrook-White formula, which gives :

$$c_b = 0.24 \tag{92}$$
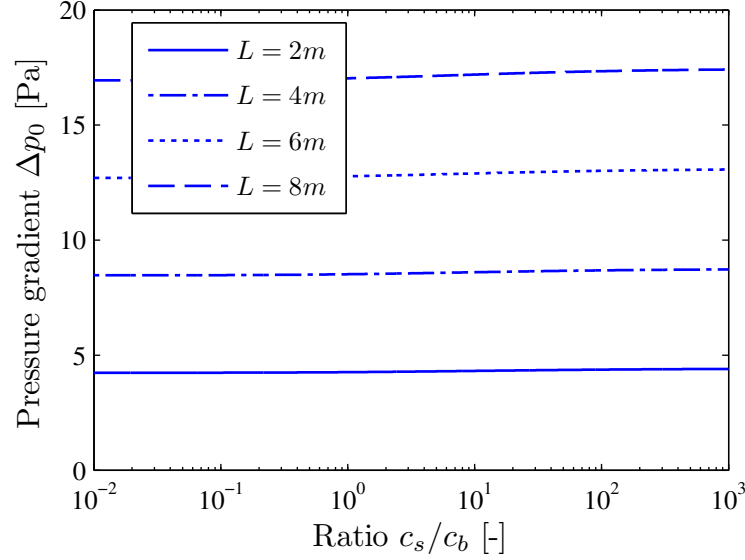
FIGURE 44 – Pressure gradient corresponding to the maximum power $\tilde{P}$ plotted with respect to the ratio c_s/c_b for various reservoir lengths

In Figure 44, it can be seen that the pressure gradient Δp_0 increases very slightly for increasing values of the ratio c_s/c_b. Moreover, when the reservoir length increases, the pressure gradient increases too. Based on the pressure gradient, it is not possible to determine the optimal ratio c_s/c_b.

In Figure 45, the ratio c_s/c_b corresponding to the maximum power $\tilde{P}$ is plotted against the Froude number F. The ratio increases when the Froude number increases. In reality, when the Froude number increases, and passes 0.21, symmetric flows become meandering flows which lead, because of oscillations, to greater interaction between the jet and the recirculation zone (higher c_s/c_b). The mathematical model is therefore consistent with what actually occurs but does not allow to clearly reproduce the change of flow regime.

FIGURE 45 – Ratio c_s/c_b corresponding to maximum power $\tilde{P}$ is displayed as a function of the Froude number F

4.5.5   Comparison between various configurations

Considering various configurations, the results obtained with mathematical and numerical models are listed in Table 8 below:
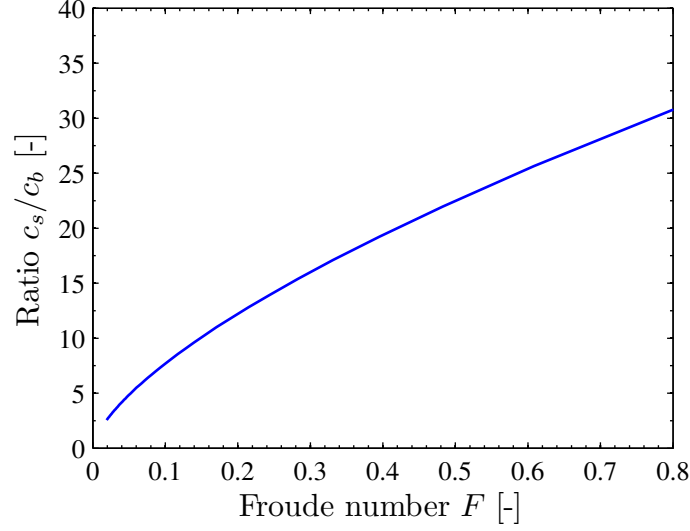
	Config. 1	Config. 2	Config.3	Config. 4
Width B $[m]$	3	4	4	4
Length L $[m]$	4	4.5	5.3	5.5
Non-dimensional power $\tilde{P}$ $[-]$	0.2847	0.4075	0.3907	0.3876
Flow $Q_{r,model}$ $[m^3/s]$	0.0064	0.0087	0.0087	0.0087
Flow $Q_{r,simulations}$ $[m^3/s]$	0.0187	0.0051	0.0050	0.0050

TABLE 8 – Comparison between various configurations

The recirculating discharge Q_r evaluated with the model depends only on the expansion ΔB (the speed ratio being almost equal), it is logical to observe an increase in flow between the first and the second configuration. However, the values obtained from the simulations show the opposite trend. To confirm these observations, other numerical simulations in which the width of expansion varies should be carried out.

It can be seen that for the same expansion ΔB, discharges obtained do not vary (or very slightly) and that, for results obtained with the mathematical model and the numerical model.

4.5.6 Conclusion

In this second model, the flow field was simplified and the velocity at the interface between the main jet and the recirculation cell was assumed to be constant contrary to the first model where it followed a parabolic distribution.

At first, the velocity field was described and the ratio between the velocity in the recirculation at the interface and the velocity in the straight jet was then evaluated based on the momentum balance equation in the recirculation zone. The non-dimensional power developed by the shear force was finally determined.

The velocity ratio, the non-dimensional power developed by the shear force and the pressure gradient were then plotted against the ratio between the shear coefficient c_s and the friction coefficient at the bottom c_b for various reservoir lengths. For increasing values of c_s/c_b, it was shown that the velocity ratio tends towards unity due to higher shear interaction between the jet and the recirculation cell. Concerning the non-dimensional power, the curve reaches a maximum which decreases with the reservoir length and is obtained for a ratio c_s/c_b that lies in the interval [5 ;15] depending on the reservoir length considered.

The velocity ratio corresponding to maximum power was then represented as a function of the reservoir length and it was demonstrated that for any length, this velocity ratio is equal to 0.6667. The pressure gradient was also displayed against the reservoir length.

The pressure gradient was also displayed against the ratio c_s/c_b for various length and it was shown that it increases when the ratio c_s/c_b or the reservoir length increases.

The influence of the Froude number on the ratio c_s/c_b was also plotted and it was shown that when the Froude number increases, the ratio also increases. This observation is consistent with the fact that in reality, when the Froude number increases, the flow is no longer symmetric but meandering. This type of flow generates a greater shear interaction and therefore a higher ratio c_s/c_b.

Finally, a comparison between the results obtained with the numerical and the mathematical models was made for various configuration. Differences could be observed in these results, however, before drawing a conclusion, it will be necessary to do new simulations WOLF2D and to compare all the numerical and analytical results again.

4.6 Asymmetric model

4.6.1 Model description

Now that the symmetric model is established and that it provides physical results, a model for representing an asymmetrical flow is developed. Based on these two models and powers obtained for each of them, it will be possible to know whether the principle of maximum power allows to determine the flow regime.

In this asymmetric model, the flow field is represented in Figure 46 and is divided into a main jet and two recirculation zones. The main jet starts from the inlet with an angle α (relative to the horizontal), comes to attach to the side wall on a distance δL and then moves towards the reservoir outlet. Its width is constant over the entire path and is equal to the inlet width b.

The first recirculation in the upper left corner is divided into three parts. Velocities in each triangle decrease linearly as they approach the center (intersection).

The second recirculation with a trapezoidal shape is composed of four triangles. In the triangles 4 and 7, velocities also decrease linearly as they approach the center. In the triangles 5 and 6, the velocity at the interface with the main jet is assumed to be identical to the one of triangle 4. In order to have an identical discharge in each triangle, a quadratic distribution of velocities is used.
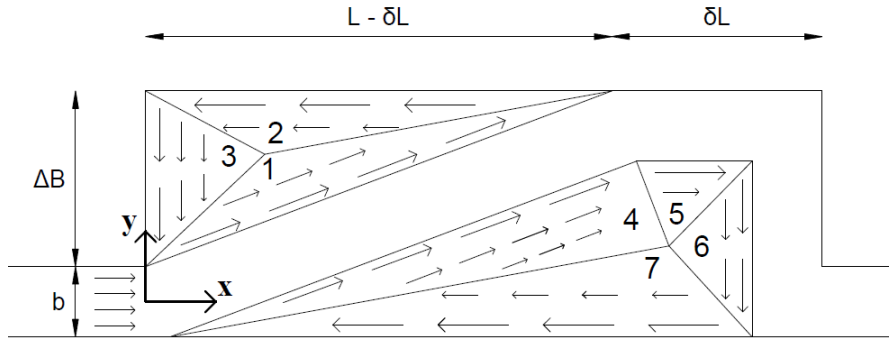

FIGURE 46 – Representation of the asymmetric model

60

Considering a local coordinate system on a triangle as shown in Figure 47, along the height of the triangle (the one starting from the center) $L_{h,i}$, the velocity for triangles 1, 2, 3, 4 and 7 is expressed as follows:

$$v_i = V_i \frac{x}{L_{h,i}} \qquad i \in [1, ..., 4, 7] \tag{93}$$

with V_i the maximum velocity in the triangle i.
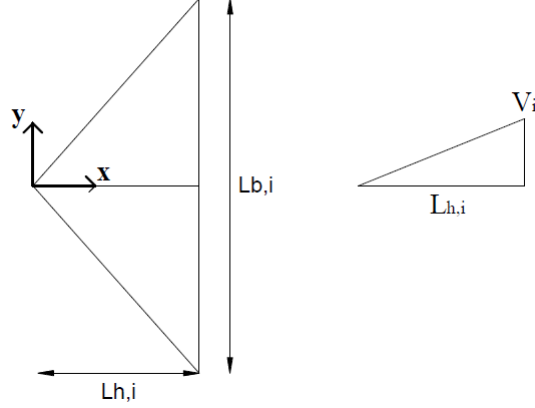
FIGURE 47 – Representation of the distribution of the velocity along the height of triangle i

Concerning triangles 5 and 6, the maximum velocities are equal to the one of triangle 4. In order to obtain the same discharge in each triangle, a quadratic distribution (Figure 48) is used and is given by the following expression:

$$v_j = V_4 \frac{x}{L_{h,j}} + V_j^* \frac{x}{L_{h,j}} (x - L_{h,j}) \qquad j \in [5, 6] \tag{94}$$
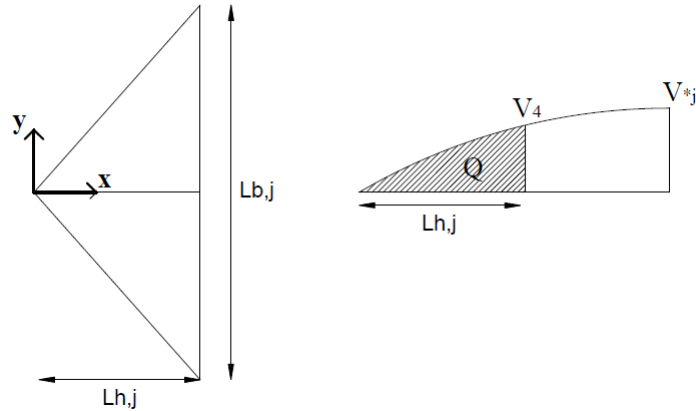

FIGURE 48 – Representation of the distribution of the velocity along the height of triangle j

Knowing that discharges Q must be the same in each triangle, it is possible to determine a

relationship between V_4 and V_j^*:

$$\int_0^{L_{h,j}} \left(V_4 \frac{x}{L_{h,j}} + V_j^* \frac{x}{L_{h,j}} \left(x - L_{h,j} \right) \right) dx = \int_0^{L_{h,4}} V_4 \frac{x}{L_{h,4}} dx \tag{95}$$

$$\left[V_4 \frac{x^2}{2L_{h,j}} + V_j^* \frac{x^3}{3L_{h,j}} - V_j^* \frac{x^2}{2} \right]_0^{L_{h,j}} = \left[V_4 \frac{x^2}{2L_{h,4}} \right]_0^{L_{h,4}} \tag{96}$$

$$\frac{1}{2} V_4 L_{h,j} - \frac{1}{6} V_j^* L_{h,j}^2 = \frac{1}{2} V_4 L_{h,4} \tag{97}$$

$$\Rightarrow V_j^* = 3V_4 \frac{L_{h,j} - L_{h,4}}{L_{h,j}^2} \tag{98}$$

Finally, the quadratic distribution writes:

$$v_j = V_4 \left[\frac{3}{L_{h,j}} \frac{L_{h,j} - L_{h,4}}{L_{h,j}^2} x^2 + \left(\frac{1}{L_{h,j}} - 3\frac{L_{h,j} - L_{h,4}}{L_{h,j}^2} \right) x \right] \qquad j \in [5,6] \tag{99}$$

4.6.2 Relations between velocities

Based on the previously established relationship between the maximum velocities of two triangles (see Appendix B.2.1):

$$V_2 = V_1 \frac{L_{h,1}}{L_{h,2}} \tag{100}$$

$$V_3 = V_1 \frac{L_{h,1}}{L_{h,3}} \tag{101}$$

The maximum velocity between triangles 4, 5 and 6 is the same and is equal to V_4 and with triangle 7, the relationship can be written as:

$$V_7 = V_4 \frac{L_{h,4}}{L_{h,7}} \tag{102}$$

4.6.3 Mass and momentum balance equations

4.6.3.1 Mass and momentum balance in the straight jet

The mass balance equation in the straight jet can be written as:

$$Q = u_0 b h \tag{103}$$

The momentum balance equation in the straight jet writes:

$$
\frac{\Delta p_0}{\rho} h b = c_b u_0^2 b L_T + c_s \left(\int_0^{L_{b,1}} [u_0 - V_1]^2 \, h dx + \int_0^{L_{b,4}} [u_0 - V_4]^2 \, h dx \right.
$$
$$
\left. + \int_0^{L_{b,5}} [u_0 - V_4]^2 \, h dx + \int_0^{L_{b,5}} [u_0 - V_4]^2 \, h dx \right) \tag{104}
$$

$$
\frac{\Delta p_0}{\rho} h b = c_b u_0^2 b L_T + c_s \left([u_0 - V_1]^2 \, h L_{b,1} + [u_0 - V_4]^2 \, h \left(L_{b,4} + L_{b,5} + L_{b,6} \right) \right) \tag{105}
$$

with

$$L_T = b/2 \tan\alpha + L_{b,1} + \delta L - b/2 + \Delta B \tag{106}$$

$$\tan\alpha = \frac{\Delta B}{L - \delta L} \tag{107}$$

4.6.3.2 Momentum balance in the first recirculation zone

The first recirculation zone (Figure 49) is split into three parts and the center is located in:

$$
\begin{aligned}
X_{O,1} &= \gamma(L - \delta L) \\
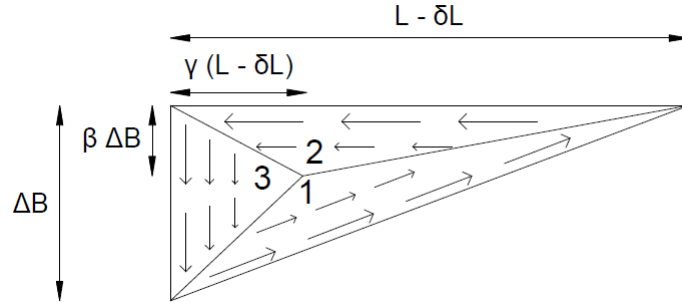Y_{O,1} &= b/2 + (1 - \beta)\Delta B
\end{aligned} \tag{108}
$$

FIGURE 49 – Recirculation zone 1 and associated notations

The associated momentum balance is given by:

$$\underbrace{\int_{S_1} c_b v_1^2(x,y)dS_1 + \int_{S_2} c_b v_2^2(y)dS_2 + \int_{S_3} c_b v_3^2(x)dS_3}_{\text{Method of triangles (see Appendix B.2.2)}} = \int_0^{L_{b,1}} c_s \left[u_0 - V_1\right]^2 hdx \qquad (109)$$

$$c_b \left(\frac{1}{4} L_{h,1} L_{b,1} V_1^2 + \frac{1}{4} L_{h,2} L_{b,2} V_2^2 + \frac{1}{4} L_{h,3} L_{b,3} V_3^2 \right) = c_s \left[u_0 - V_1\right]^2 h L_{b,1} \qquad (110)$$

$$\frac{1}{4} c_b V_1^2 \underbrace{\left(L_{h,1} L_{b,1} + L_{h,1}^2 \frac{L_{b,2}}{L_{h,2}} + L_{h,1}^2 \frac{L_{b,3}}{L_{h,3}} \right)}_{C_1} = c_s \left[u_0 - V_1\right]^2 h L_{b,1} \qquad (111)$$

with $L_{b,i}$ which represents the length of the base of triangle i and is also the length of the side opposite to the angle formed at the intersection/center.

The relationship between V_1 and u_0 can be obtained by developing the equation above:

$$\frac{V_1}{u_0} = \frac{-\frac{c_s}{c_b} \pm \sqrt{\frac{1}{4}\frac{c_s}{c_b}C_1}}{\left[\frac{1}{4}C_1 - \frac{c_s}{c_b}\right]} \qquad (112)$$

4.6.3.3 Momentum balance in the second recirculation zone

The second recirculation zone is represented in Figure 50 and the common apex of the four triangles is in $(X_{O,2}\,;\,Y_{O,2})$.
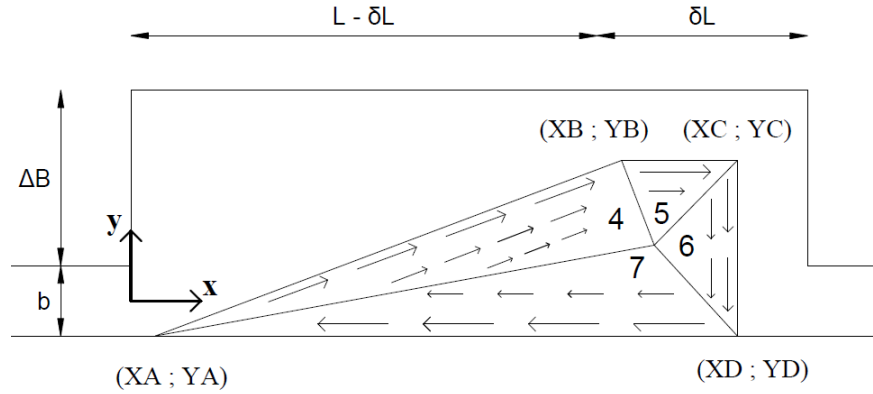

FIGURE 50 – Recirculation zone 2 and associated notations

The coordinates of the four corners are:

$$\begin{array}{ll} X_A = d & ;\ Y_A = -b/2 \\ X_B = L - \delta L + d & ;\ Y_B = \Delta B - b/2 \\ X_C = L - b & ;\ Y_C = \Delta B - b/2 \\ X_D = L - b & ;\ Y_D = -b/2 \end{array} \qquad (113)$$

with

$$d = b \tan \alpha \tag{114}$$

In this recirculation zone, the momentum balance is expressed as follows:

$$c_b \underbrace{\left[\int_{S_1} v_1^2(x, y) dS_1 + \int_{S_2} v_2^2(y) dS_2 + \int_{S_3} v_3^2(x) dS_3 + \int_{S_4} v_4^2(x) dS_4 \right]}_{\text{Method of triangles and function } int \text{ in Matlab}}$$
$$= c_s \left(\int_0^{L_{b,4}} [u_0 - V_4]^2 \, h dx + \int_0^{L_{b,5}} [u_0 - V_4]^2 \, h dx + \int_0^{L_{b,5}} [u_0 - V_4]^2 \, h dx \right) \tag{115}$$

4.6.4 Power developed by the shear force

The power developed by the shear force is given by:

$$P = c_s h \int_0^{L_{b,1}} (u_0 - V_1)^2 (u_0 - V_1) \, dx + c_s h \int_0^{L_{b,4}} (u_0 - V_4)^2 (u_0 - V_4) \, dx$$
$$+ c_s h \int_0^{L_{b,5}} (u_0 - V_4)^2 (u_0 - V_4) \, dx + c_s h \int_0^{L_{b,6}} (u_0 - V_4)^2 (u_0 - V_4) \, dx \tag{116}$$
$$= c_s h \left[(u_0 - V_1)^3 L_{b,1} + (u_0 - V_4)^3 L_{b,4} + (u_0 - V_4)^3 L_{b,5} + (u_0 - V_4)^3 L_{b,6} \right] \tag{117}$$
$$= c_s h \left[(u_0 - V_1)^3 L_{b,1} + (u_0 - V_4)^3 (L_{b,4} + L_{b,5} + L_{b,6}) \right] \tag{118}$$

The non-dimensional form writes:

$$\tilde{P} = \frac{P}{c_b h L_{b,1} u_0^3} \tag{119}$$
$$= \frac{c_s}{c_b} \left[\left(1 - \frac{V_1}{u_0} \right)^3 + \frac{L_{b,4} + L_{b,5} + L_{b,6}}{L_{b,1}} \left(1 - \frac{V_4}{u_0} \right)^3 \right] \tag{120}$$

4.6.5 Results and discussion

Data used to represent the results obtained with these equations are:

$$B = 3.00m; b = 0.25m; \delta L = \frac{1}{3}L; \gamma = \frac{1}{4}; \beta = \frac{1}{4} \tag{121}$$

The two velocity ratios V_1/u_0 and V_4/u_0 are plotted with respect to the ratio c_s/c_b for various reservoir lengths in Figure 51. As for the symmetric model, the two velocity ratios tends towards unity for increasing values of c_s/c_b corresponding to a higher shear interaction. For a given ratio c_s/c_b, the velocity ratio in the trapezoidal recirculation zone V_4/u_0 is higher than the velocity ratio in the triangular recirculation cell V_1/u_0.
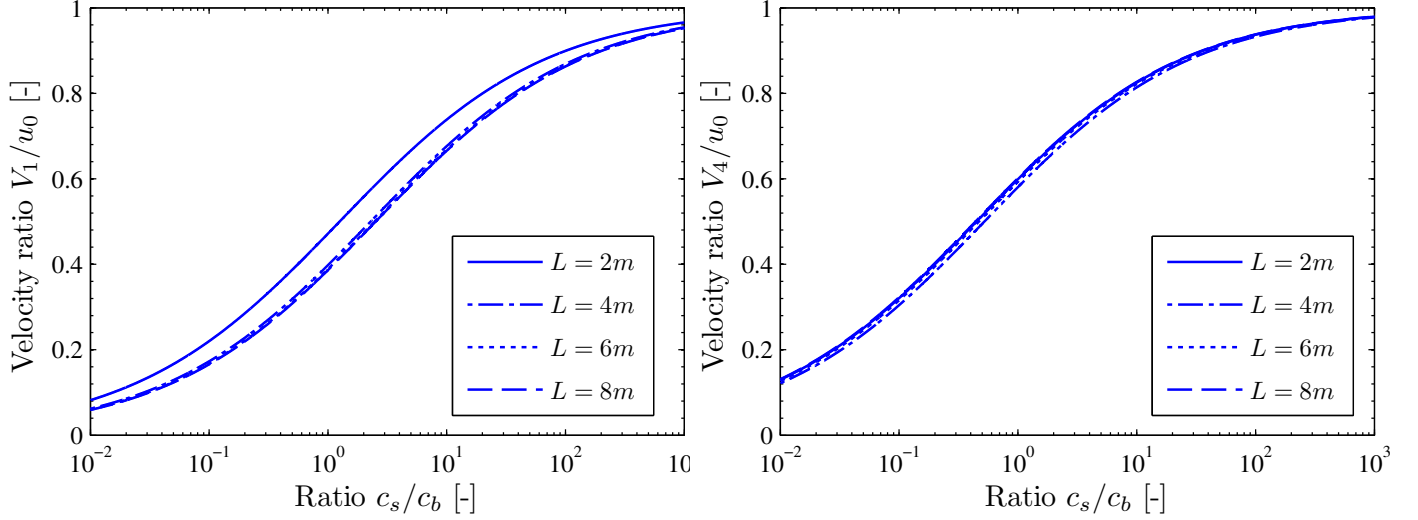

FIGURE 51 – Velocity ratios V_1/u_0 (left) and V_4/u_0 (right) plotted against the ratio c_s/c_b for various reservoir lengths

The non-dimensional power $\tilde{P}$ reaches a maximum, which increases with the reservoir length (Figure 52).
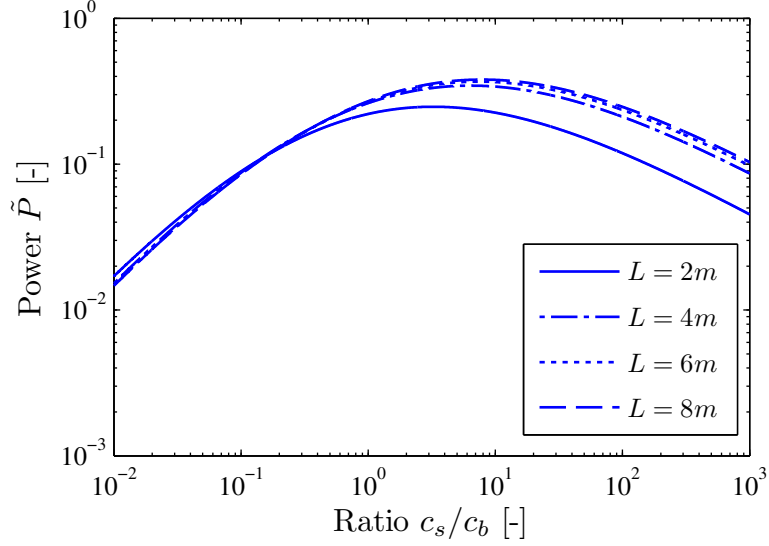
FIGURE 52 – Evolution of the non-dimensional power $\tilde{P}$ as a function of the ratio c_s/c_b for various lengths

The evolution of the two velocity ratios corresponding to maximum non-dimensional power $\tilde{P}$ are plotted as a function of the reservoir lengths in Figure 53. In the two cases, the velocity ratio increases as the reservoir length increases. The ratio V_4/u_0 is at any point greater than the ratio V_1/u_0, which is surely due to the fact that the length of the shear interface for the second recirculation (trapezoidal) is higher than for the first recirculation (triangular).

FIGURE 53 – Evolution of the two velocity ratios plotted with respect to the reservoir length L

4.6.6 Conclusion

In this subsection, the development of a mathematical model for representing the phenomena associated with an asymmetric flow is achieved. The flow field is divided into a main jet and two recirculation zones (one triangular and one trapezoidal).

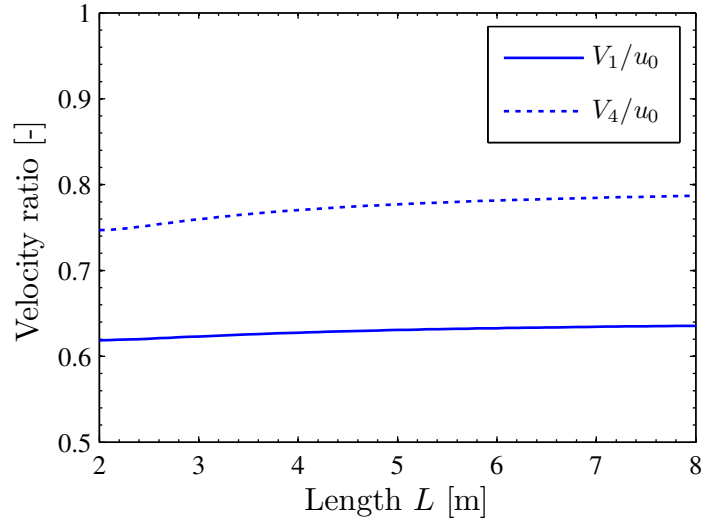At first, the velocity distributions in the recirculation zones are determined. The two velocity ratios are then evaluated based on the momentum balance equations developed for each recirculation zone. The non-dimensional power developed by the shear force is finally computed using the two velocity ratios.

The two velocity ratios and the non-dimensional power were displayed as a function of the ratio between the shear coefficient c_s and the friction coefficient at the bottom c_b for various reservoir lengths. With regard to the velocity ratios, the observations are the same as for the previous symmetric model, namely that when the ratio c_s/c_b increases, the velocity ratio tends towards unity. Moreover, the velocity ratio of the trapezoidal recirculation cell is higher than the one of the triangular recirculation zone which is due to the greater shear interaction length. Concerning the non-dimensional power, as for the symmetric model, it reaches a maximum for a ratio c_s/c_b which varies between 5 and 15 but contrary to this symmetric model, the maximum increases when the reservoir length increases.

The influence of the reservoir length on the velocity ratios was then studied. It was shown that for increasing values of the reservoir length, the two velocity ratios increases, the velocity ratio in the trapezoidal recirculation zone being at every point greater that the one of the triangular zone and increasing more quickly with the reservoir length.

4.7 Comparison between the symmetric and the asymmetric model

4.7.1 Introduction

Now that both models (symmetric and asymmetric) were developed, they will be compared to know whether the principle of maximum power (see State of the art) can be used to determine the flow regime in the reservoir.

4.7.2 Comparison

In Figure 54, the maximum of the non-dimensional power $\tilde{P}$ represented against the Shape Factor SF for the symmetric and asymmetric models. Data used are the same as for the previous model:

$$B = 3.00m; b = 0.25m; \delta L = \frac{1}{3}L; \gamma = \frac{1}{4}; \beta = \frac{1}{4} \tag{122}$$

FIGURE 54 – Maximum of the non-dimensional power $\tilde{P}$ plotted with respect to the Shape Factor SF for the symmetric and asymmetric models

In the symmetric model, the maximum of the non-dimensional power $\tilde{P}$ decreases when the Shape Factor increases while for the asymmetric model, the power $\tilde{P}$ increases.

Based on the principle of maximum power, it can be seen that for $SF < 4.05$, the flow is symmetric and when $SF > 4.05$, the flow becomes asymmetric. This is consistent with the experimental results (see the state of the art). However, the boundary obtained with the model does not match with the one of the experimental results which is between $6.2 - 8.1$.

By modifying the geometric parameters, it is possible to modify the curve obtained from

the asymmetric model. The Figure 55 shows the comparison between the two models consi-dering the following parameters :

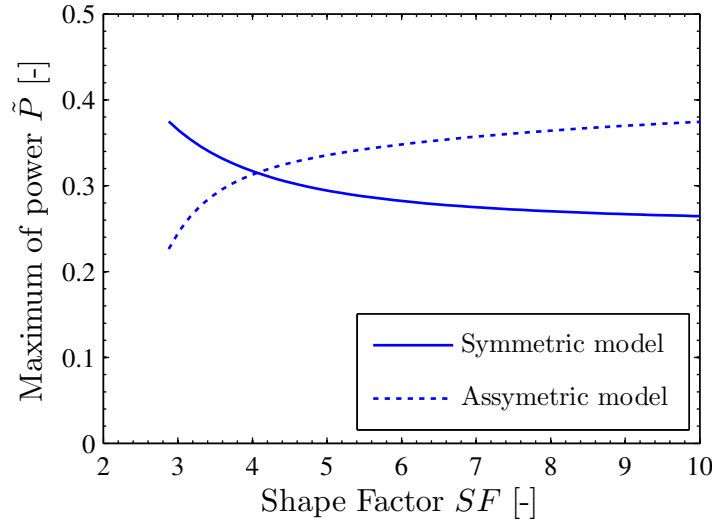$$B = 3.00m; b = 0.25m; \delta L = \frac{1}{4}L; \gamma = 0.29; \beta = 0.29 \tag{123}$$
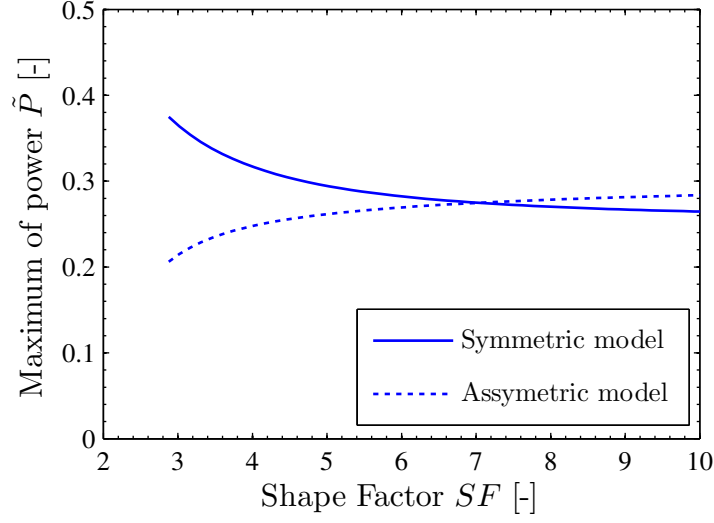
FIGURE 55 – Maximum of the non-dimensional power $\tilde{P}$ plotted with respect to the Shape Factor SF for the symmetric and asymmetric models considering other geometric data

With these geometric parameters, the boundary between the symmetric and asymmetric flows corresponds to a Shape Factor SF equals to 7 ($\in [6.2 - 8.1]$).

Let's look now if the data used are consistent with what can be observed numerically. In Figure 56, an asymmetric flow obtained with WOLF2D byCamnasio et al. (2014) is repre-sented. The configuration has a width of 2m and a length of 4m. The center of the triangular recirculation zone is represented by a red circle.

FIGURE 56 – Simulation of an asymmetric flow using WOLF2D obtained by Camnasio et al. (2014)

The parameters associated with this simulation are :

$$\delta L = 0.4L; \gamma = 0.5; \beta = 0.4 \tag{124}$$

By comparing the two set of parameters, it can be seen that they are quite different. However, this first approach is mainly qualitative and shows if the results obtained with the analytic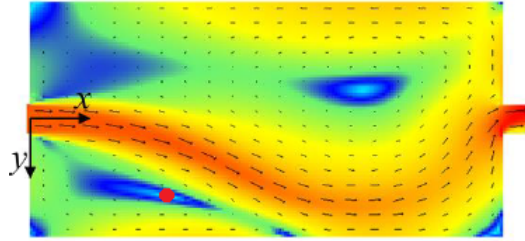al model are physical. In the future, a complete model incorporating the two lateral expansions (and not only one) will need to be studied and the parameters obtained will be compared with those obtained numerically.

4.7.3 Conclusion

In this section, a comparison between symmetric and asymmetric models, and more specifically, on the non-dimensional power developed by each model was performed.

It was shown that for increasing values of the Shape Factor, the maximum of the non-dimensional power developed by the shear force decreases for the symmetric model while it increases for the asymmetric model, which leads to an intersection between the two curves. Based on the principle of maximum power, all flows occurring in a configuration with a lower Shape Factor than the Shape Factor corresponding to the intersection, are symmetric while when it exceeds this limit (intersection), the flows are asymmetric.

It was also demonstrated that the geometric parameters such as the length of attachment or the center of the triangular recirculation zone in the case of asymmetric model influences the shape of the curve and therefore, the position of the intersection.

A comparison between the parameters such as the position of the center of the recirculation or the reattachment length obtained numerically and analytically was performed. Differences were observed, however, in order to realize a complete and correct comparison, it will be necessary to develop analytical models with two lateral expansions.

4.8   Conclusion

This section focuses on the development of two analytical models to represent symmetric and asymmetric flows. The applicability of the principle of maximum power is also discussed.

In each model developed, the mass and momentum balance equations were expressed and were used to determine the ratio between velocities in the main jet and the recirculation zones, the non-dimensional power developed by the shear force and the pressure gradient.

Both models can reproduce physical phenomena such as the fact that when the shear interaction between the main jet and the recirculation cell increases, the velocity in the recirculation zone near the interface with the main jet tends to the velocity of the jet.

It was also shown that in both models the power curve has a maximum, which when the flow is symmetric decreases with reservoir length while it increases for asymmetric flow.

By comparing the powers obtained for each model, it was demonstrated that the principle of maximum power can be used to determine the flow regime occurring in a configuration with a given geometry.

All the observations and results obtained here are only qualitative. Differences between results obtained with the analytical and the numerical models were indeed identified. Subsequently, these models should be improved to fully represent the phenomena occurring in shallow reservoirs.

5   Conclusion

The aim of this Master's thesis was to enhance the knowledge of the different flow regimes occurring in shallow reservoirs to improve the reservoir management.

Thus, the first part of this thesis was devoted to the study of meandering flows and more specifically, the influence of the reservoir geometry on the main characteristics of this type of flow. The experimental protocol was first validated through experiments performed for an previously studied configuration. Two further experiments were then conducted to determine the impact of the geometric factors of the reservoir such as its length or its width on the main characteristics of meandering flows (frequency, characteristic lengths). Large-Scale PIV was used to measure the surface flow fields and a Proper Orthogonal Decomposition was applied on these fields to extract the results. Finally, it was shown that for a given regime flow which depends on the Froude number and the Shape Factor, the main properties of the flow does not depend on the reservoir geometry but on its shallowness.

The second part of this thesis focused on the development of two analytical models used to represent phenomenon occurring in symmetric and asymmetric flows. The applicability of the principle of maximum power was also discussed. For each model, the mass and momentum balance equations were established and the power developed by the shear force at the interface between the main jet and recirculation zones was determined. By comparing the powers obtained for each model, it was demonstrated that the maximum power principle can be used to predict the flow regime occurring in a reservoir with a given geometric configuration.

Nevertheless, it still remains work to improve the knowledge of hydrodynamic flows in shallow reservoirs:

- Boundaries between the different flows regimes are not well defined and need to be studied,

- Both analytical models developed should be improved to provide results similar to those obtained numerically,

- Once the 2D models will be established, they could be extended in 3D.

Bibliography

Andrianne, T. and Dimitriadis, G. (2012). Damping identification of lightly damped linear dynamic systems using common-base proper orthogonal decomposition. *Mechanical Systems and Signal Processing*, 28 :492–506. cited By 4.

Camnasio, E., Erpicum, S., Archambeau, P., Pirotton, M., and Dewals, B. (2014). Prediction of mean and turbulent kinetic energy in rectangular shallow reservoirs. *Engineering Applications of Computational Fluid Mechanics*, 8(4) :586–597. cited By 0.

Camnasio, E., Orsi, E., and Schleiss, A. (2011). Experimental study of velocity fields in rectangular shallow reservoirs. *Journal of Hydraulic Research*, 49(3) :352–358. cited By 10.

Choi, S.-U. and Garcia, M. (2002). $k - \varepsilon$ turbulence modeling of density currents developing two dimensionally on a slope. *Journal of Hydraulic Engineering*, 128(1) :55–63. cited By 60.

Chu, V., Liu, F., and Altai, W. (2004). Friction and confinement effects on a shallow recirculating flow. *Journal of Environmental Engineering and Science*, 3(5) :463–475. cited By 17.

Dewals, B., Kantoush, S., Erpicum, S., Pirotton, M., and Schleiss, A. (2008). Experimental and numerical analysis of flow instabilities in rectangular shallow basins. *Environmental Fluid Mechanics*, 8(1) :31–54. cited By 44.

Dracos, T., Giger, M., and Jirka, G. (1992). Plane turbulent jets in a bounded fluid layer. *JOURNAL OF FLUID MECHANICS*, 241 :587–614. cited By 64.

Dufresne, M., Dewals, B., Erpicum, S., Archambeau, P., and Pirotton, M. (2010). Classification of flow patterns in rectangular shallow reservoirs. *Journal of Hydraulic Research*, 48(2) :197–204. cited By 13.

Dufresne, M., Dewals, B., Erpicum, S., Archambeau, P., and Pirotton, M. (2012). Flow patterns and sediment deposition in rectangular shallow reservoirs. *Water and Environment Journal*, 26(4) :504–510. cited By 5.

Erpicum, S., Meile, T., Dewals, B., Pirotton, M., and Schleiss, A. (2009). 2d numerical flow modeling in a macro-rough channel. *International Journal for Numerical Methods in Fluids*, 61(11) :1227–1246. cited By 22.

Kantoush, S., S., Bollaert, E., and Schleiss, A. (2008). Experimental and numerical modelling of sedimentation in a rectangular shallow basin. *International Journal of Sediment Research*, 23(3) :212–232. cited By 16.

Kolár, V. (2007). Vortex identification : New requirements and limitations. *International Journal of Heat and Fluid Flow*, 28(4) :638–652. cited By 55.

Muste, M., Fujita, I., and Hauet, A. (2010). Large-scale particle image velocimetry for measurements in riverine environments. *Water Resources Research*, 46(4). cited By 0.

Paltridge, G. (1979). Climate and thermodynamic systems of maximum dissipation. *Nature*, (279) :630–631.

Peltier, Y., Erpicum, S., Archambeau, P., Pirotton, M., and Dewals, B. (2014a). Experimental investigation of meandering jets in shallow reservoirs. *Environmental Fluid Mechanics*, 14(3) :699–710. cited By 3.

Peltier, Y., Erpicum, S., Archambeau, P., Pirotton, M., and Dewals, B. (2014b). Meandering jets in shallow rectangular reservoir. pages 21–29. cited By 0.

Peltier, Y., Erpicum, S., Archambeau, P., Pirotton, M., and Dewals, B. (2014c). Meandering jets in shallow rectangular reservoirs : Pod analysis and identification of coherent structures. *Experiments in Fluids*, 55(6). cited By 1.

Peltier, Y., Erpicum, S., Archambeau, P., Pirotton, M., and Dewals, B. (2015). Can meandering flows in shallow rectangular reservoirs be modeled with the 2d shallow water equations ? *Journal of Hydraulic Engineering*, 141, 04015008.

Schymanski, S. J., Sivapalan, M., Roderick, M. L., Hutley, L. B., and Beringer, J. (2009). An optimality-based model of the dynamic feedbacks between natural vegetation and the water balance. *Water Resources Research*, 45.

Thielicke, W. and Stamhuis, E. J. (2014). Pivlab − towards user-friendly, affordable and accurate digital particle image velocimetry in matlab. *Journal of Open Research Software*, 2(1) :2049–9647.

Westhoff, M. and Zehe, E. (2013). Maximum entropy production : Can it be used to constrain conceptual hydrological models ? *Hydrology and Earth System Sciences*, 17(8) :3141–3157. cited By 4.

Appendix

A   Experimental part

A.1   Configuration 1

A.1.1   POD analysis - Comparison

Temporal coefficients

The temporal coefficients obtained from the eigenvectors of the five first modes are represented in Figure 57 for a discharge Q of 0.25 L/s, and this for the data collected by Peltier Y. (2012-2013) and the present data.
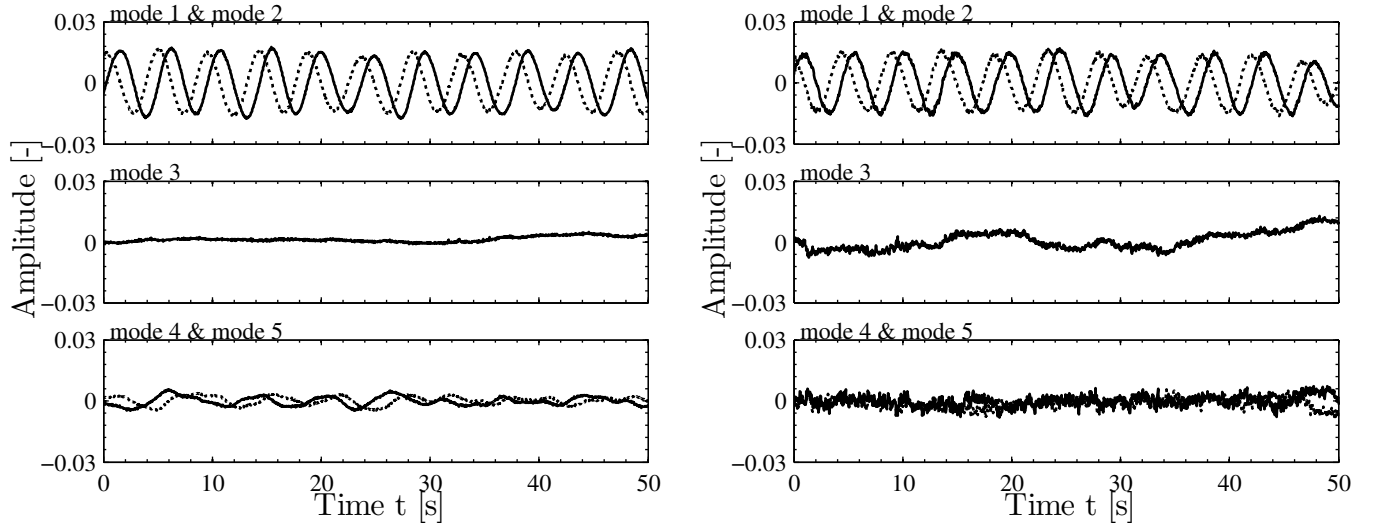

FIGURE 57 – Representation of the temporal coefficients of the five first mode corresponding to $Q = 0.25$ L/s for Peltier's data (left) and present data (right) - The *solid lines* represent odd modes and the *dotted lines* even modes

The results obtained with the Modal Assurance Criterion (MAC) are represented in Figure 58.

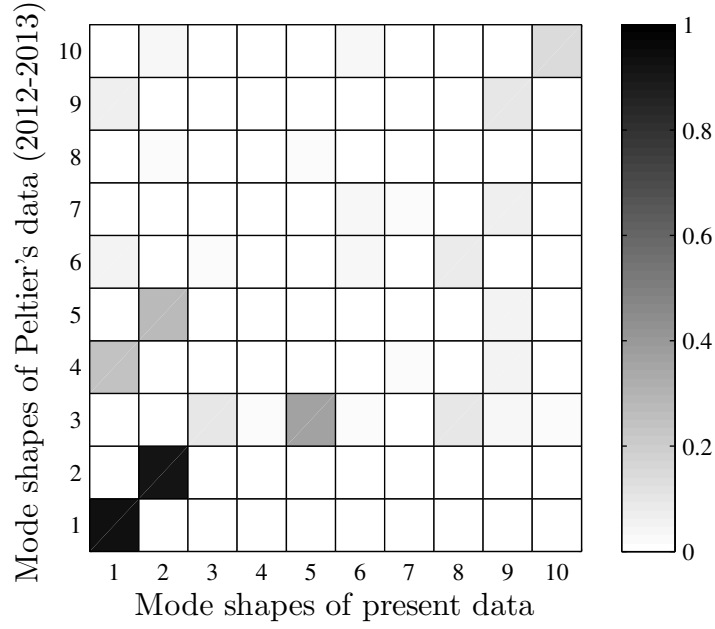FIGURE 58 – Comparison between Peltier's data (2012-2013) and present data using MAC matrix

The first two modes have a correlation close to unity.

Spatial modes

The first five spatial modes corresponding to a discharge Q of 0.50 L /s are displayed in Figure 59 for Peltier's data (2012-2013) and in Figure 60 for present data.

The same conclusions as those drawn for a discharge Q of 0.25 L/s can be done.
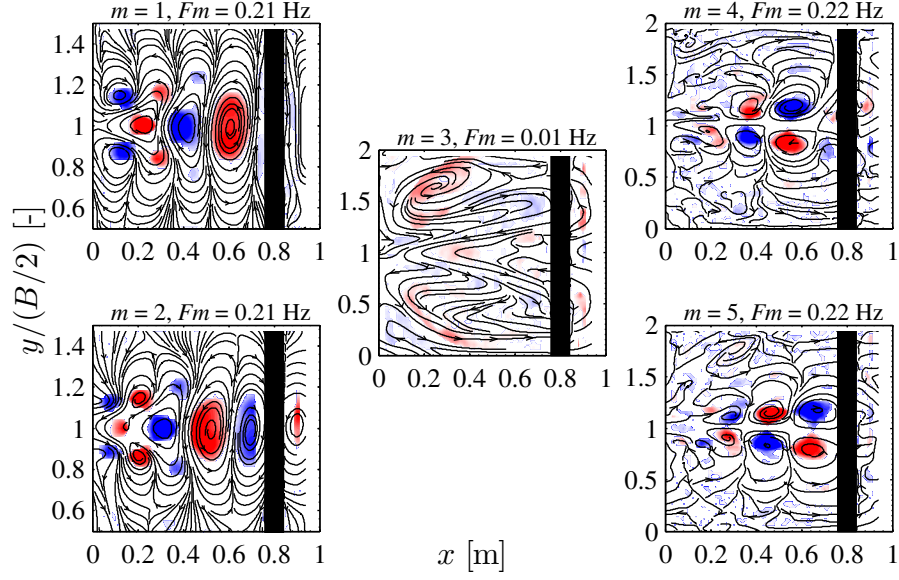
FIGURE 59 – Representation of the first five spatial modes for Q equals to 0.25 L/s based on Peltier's data (2012-2013) - The *black rectangle* corresponds to a blank zone during the measurement - When the vorticity is negative, it is represented in blue while it is in red when it is positive
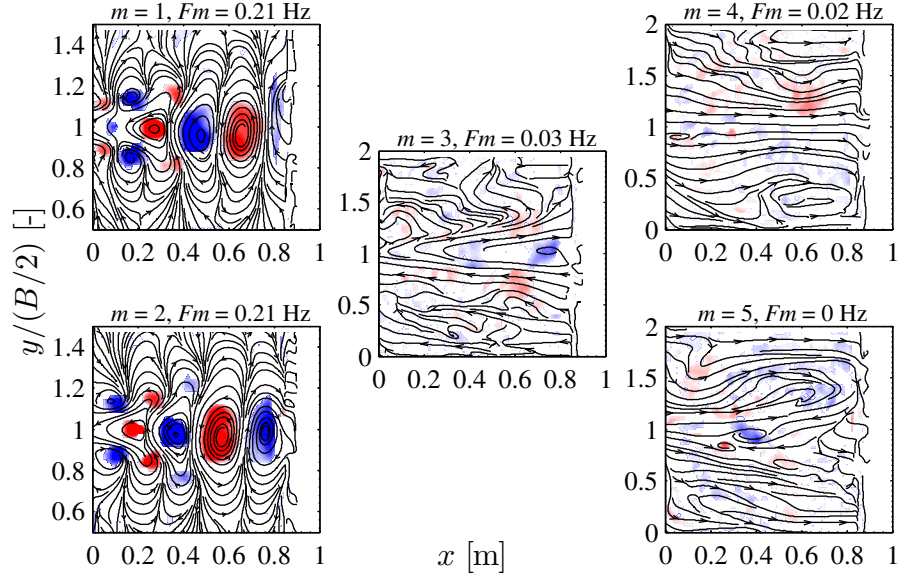

FIGURE 60 – Representation of the first five spatial modes for Q equals to 0.25 L/s based on present data - The *empty area* corresponds to an inaccessible area due to the camera position

B Mathematical developments

B.1 Mathematical model N°1

B.1.1 General approach - Speed ratio

$$C_b u_L^2 = C_s \left(u - u_L \right)^2 \tag{125}$$

$$C_b u_L^2 = C_s \left(u^2 - 2u u_L + u_L^2 \right) \tag{126}$$

$$\left(C_b - C_s \right) u_L^2 + 2 C_s u u_L - C_s u^2 = 0 \tag{127}$$

$$u_L^2 + 2 \frac{C_s}{C_b - C_s} u u_L - \frac{C_s}{C_b - C_s} u^2 = 0 \tag{128}$$

$$u_L = - \frac{C_s}{C_b - C_s} u \pm \sqrt{\left(\frac{C_s}{C_b - C_s} u \right)^2 + \frac{C_s}{C_b - C_s} u^2} \tag{129}$$

$$\frac{u_L}{u} = - \frac{C_s}{C_b - C_s} \pm \sqrt{\frac{C_s^2 + C_s \left(C_b - C_s \right)}{\left(C_b - C_s \right)^2}} \tag{130}$$

$$\frac{u_L}{u} = - \frac{C_s}{C_b - C_s} \pm \sqrt{\frac{C_s C_b}{\left(C_b - C_s \right)^2}} \tag{131}$$

$$\frac{u_L}{u} = \frac{-C_s \pm \sqrt{C_s C_b}}{C_b - C_s} \tag{132}$$

$$\frac{u_L}{u} = \frac{-\frac{C_s}{C_b} \pm \sqrt{\frac{C_s}{C_b}}}{1 - \frac{C_s}{C_b}} \tag{133}$$

B.1.2 General approach - Power of the shear force

$$\tilde{P} = \frac{P}{C_b u^3} \tag{134}$$

$$= \frac{C_s}{C_b} \left(1 - \frac{u_L}{u} \right)^3 \tag{135}$$

$$= \frac{C_s}{C_b} \left(1 - \frac{-C_s \pm \sqrt{C_s C_b}}{C_b - C_s} \right)^3 \tag{136}$$

$$= \frac{C_s}{C_b} \left(\frac{C_b \mp \sqrt{C_s C_b}}{C_b - C_s} \right)^3 \tag{137}$$

$$= \frac{C_s}{C_b} \left(\frac{1 \mp \sqrt{\frac{C_s}{C_b}}}{1 - \frac{C_s}{C_b}} \right)^3 \tag{138}$$

B.1.3 Relation between V_0 and $\tilde{V}_0$

$$\int_{\frac{b}{2}}^{\frac{b+\Delta B}{2}} u_\omega(L/2, y) dy = \int_{\frac{L}{2}}^{L} v_\omega(x, b/2 + \Delta B/2) dx \tag{139}$$

$$\int_{\frac{b}{2}}^{\frac{b+\Delta B}{2}} -V_0 \frac{2}{\Delta B} \left(y - \frac{b+\Delta B}{2} \right) dy = \int_{\frac{L}{2}}^{L} \tilde{V}_0 \left(x - \frac{L}{2} \right) \frac{2}{L} dx \tag{140}$$

$$-V_0 \frac{2}{\Delta B} \left[\frac{y^2}{2} - \frac{b+\Delta B}{2} y \right]_{\frac{b}{2}}^{\frac{b+\Delta B}{2}} = \tilde{V}_0 \frac{2}{L} \left[\frac{x^2}{2} - \frac{L}{2} x \right]_{\frac{L}{2}}^{L} \tag{141}$$

$$-V_0 \frac{2}{\Delta B} \left[\frac{1}{2} \left(\frac{b+\Delta B}{2} \right)^2 - \frac{1}{2} \left(\frac{b}{2} \right)^2 - \frac{b+\Delta B}{2} \frac{\Delta B}{2} \right] = \tilde{V}_0 \frac{2}{L} \left[\frac{1}{2} \left(L^2 - \frac{L^2}{4} \right) - \frac{L^2}{4} \right] \tag{142}$$

$$-V_0 \frac{1}{\Delta B} \left[\frac{b^2}{4} + \frac{b\Delta B}{2} + \frac{\Delta B^2}{4} - \frac{b^2}{4} - \frac{b\Delta B}{2} - \frac{\Delta B^2}{2} \right] = \tilde{V}_0 \frac{1}{L} \left[\frac{3L^2}{4} - \frac{L^2}{2} \right] \tag{143}$$

$$-V_0 \frac{1}{\Delta B} \frac{-\Delta B^2}{4} = \tilde{V}_0 \frac{1}{L} \frac{L^2}{4} \tag{144}$$

$$V_0 \Delta B = \tilde{V}_0 L \tag{145}$$

$$\boxed{\tilde{V}_0 = \frac{\Delta B}{L} V_0} \tag{146}$$

B.1.4 Momentum balance equation in the straight jet

$$\int_0^L c_s \left[u_0 - u_\omega \left(x, \frac{b}{2} \right) \right]^2 h dx \tag{147}$$

$$= c_s h \int_0^L \left[u_0 - 4V_0 \left(\frac{b}{\Delta B} + 1 - \frac{2b}{2\Delta B} \right) \left(1 - \frac{x}{L} \right) \frac{x}{L} \right]^2 dx \tag{148}$$

$$\overset{(*)}{=} c_s h V_0^2 L \int_0^1 \left[\frac{u_0}{V_0} - 4 \left(1 - \beta \right) \beta \right]^2 d\beta \tag{149}$$

$$= c_s h V_0^2 L \int_0^1 \left[\frac{u_0}{V_0} - 4\beta + 4\beta^2 \right]^2 d\beta \tag{150}$$

$$= c_s h V_0^2 L \int_0^1 \left[\left(\frac{u_0}{V_0} \right)^2 + 16\beta^2 + 16\beta^4 - 8 \left(\frac{u_0}{V_0} \right) \beta + 8 \left(\frac{u_0}{V_0} \right) \beta^2 - 32\beta^3 \right] d\beta \tag{151}$$

$$= c_s h V_0^2 L \int_0^1 \left[\left(\frac{u_0}{V_0} \right)^2 - 8 \left(\frac{u_0}{V_0} \right) \beta + \left(16 + 8 \left(\frac{u_0}{V_0} \right) \right) \beta^2 - 32\beta^3 + 16\beta^4 \right] d\beta \tag{152}$$

$$= c_s h V_0^2 L \left[\left(\frac{u_0}{V_0} \right)^2 \beta - 4 \left(\frac{u_0}{V_0} \right) \beta^2 + \frac{1}{3} \left(16 + 8 \left(\frac{u_0}{V_0} \right) \right) \beta^3 - 8\beta^4 + \frac{16}{5} \beta^5 \right]_0^1 \tag{153}$$

$$= c_s h V_0^2 L \left[\left(\frac{u_0}{V_0} \right)^2 - 4 \left(\frac{u_0}{V_0} \right) + \frac{1}{3} \left(16 + 8 \left(\frac{u_0}{V_0} \right) \right) - 8 + \frac{16}{5} \right] \tag{154}$$

$$= c_s h V_0^2 L \left[\left(\frac{u_0}{V_0} \right)^2 - \frac{4}{3} \left(\frac{u_0}{V_0} \right) + \frac{8}{15} \right] \tag{155}$$

$$= c_s h L \left[u_0^2 - \frac{4}{3} u_0 V_0 + \frac{8}{15} V_0^2 \right] \tag{156}$$

$(*)$ We assume that : $\frac{x}{L} = \beta$

B.1.5 Momentum balance equation in the recirculation

$$\int_S c_b \omega^2(x,y)dS \tag{157}$$

$$= \int_{\frac{b}{2}}^{\frac{b}{2}+\Delta B} \int_0^L c_b \left(u_\omega^2 + v_\omega^2\right) dxdy \tag{158}$$

$$= \int_{\frac{b}{2}}^{\frac{b}{2}+\Delta B} \int_0^L c_b \left[16V_0^2 \left(\frac{b}{\Delta B} + 1 - \frac{2y}{\Delta B}\right)^2 \left(1 - \frac{x}{L}\right)^2 \left(\frac{x}{L}\right)^2 \right.$$
$$\left. + 16V_0^2 \left(\frac{\Delta B}{L}\right)^2 \left(\frac{b}{2\Delta B} - \frac{y}{\Delta B}\right)^2 \left(\frac{y}{\Delta B} - \frac{b}{2\Delta B} - 1\right)^2 \left(\frac{2x}{L} - 1\right)^2 \right] dxdy \tag{159}$$

$$\overset{(*)}{=} 16c_b V_0^2 \Delta B L \int_{C_1}^{C_1+1} \int_0^1 \left[(2C_1 + 1 - 2\beta)^2 (1-\alpha)^2 \alpha^2 \right.$$
$$\left. + \left(\frac{\Delta B}{L}\right)^2 (C_1 - \beta)^2 (\beta - C_1 - 1)^2 (2\alpha - 1)^2 \right] d\alpha d\beta \tag{160}$$

$$= 16c_b V_0^2 \Delta B L \int_{C_1}^{C_1+1} \int_0^1 \left[a_1 \left(\alpha^4 - 2\alpha^3 + \alpha^2\right) + a_2 \left(4\alpha^2 - 4\alpha + 1\right) \right] d\alpha d\beta \tag{161}$$

$$= 16c_b V_0^2 \Delta B L \int_{C_1}^{C_1+1} \left[a_1 \frac{\alpha^5}{5} - 2a_1 \frac{\alpha^4}{4} + (a_1 + a_2)\frac{\alpha^3}{3} - 4a_2 \frac{\alpha^2}{2} + a_2\alpha \right]_0^1 d\beta \tag{162}$$

$$= 16c_b V_0^2 \Delta B L \int_{C_1}^{C_1+1} \left[\frac{1}{30} (2C_1 + 1 - 2\beta) - \frac{2}{3}\left(\frac{\Delta B}{L}\right)^2 (C_1 - \beta)^2 (\beta - C_1 - 1)^2 \right] d\beta \tag{163}$$

$$= 16c_b V_0^2 \Delta B L \left[\frac{\Delta B^2}{90L^2} + \frac{1}{90} \right] \tag{164}$$

$$= \frac{8}{45} c_b V_0^2 \Delta B L \left[\frac{\Delta B^2}{L^2} + 1 \right] \tag{165}$$

$(*)$ We assume that :

$$\alpha = \frac{x}{L} \ ; \ \beta = \frac{y}{\Delta B} \ ; \ C_1 = \frac{b}{2\Delta B} \tag{166}$$

B.1.6 Speed ratio V_0/u_0

$$\frac{8}{45} c_b V_0^2 \Delta B \left[\frac{\Delta B^2}{L^2} + 1 \right] = c_s h \left[u_0^2 - \frac{4}{3} u_0 V_0 + \frac{8}{15} V_0^2 \right] \tag{167}$$

$$V_0^2 \left[\frac{8}{45} c_b \Delta B \left(\frac{\Delta B^2}{L^2} + 1 \right) - \frac{8}{15} c_s h \right] + \frac{4}{3} c_s h u_0 V_0 - c_s h u_0^2 = 0 \tag{168}$$

$$\Rightarrow V_0 = \frac{-\frac{4}{3} c_s h u_0 \pm \sqrt{ -\frac{16}{45} c_s^2 h^2 u_0^2 + \frac{32}{45} c_b c_s \Delta B h \left(\frac{\Delta B^2}{L^2} + 1 \right) u_0^2 }}{2 \left[\frac{8}{45} c_b \Delta B \left(\frac{\Delta B^2}{L^2} + 1 \right) - \frac{8}{15} c_s h \right]} \tag{169}$$

$$\Leftrightarrow \frac{V_0}{u_0} = \frac{-\frac{1}{3} \frac{c_s}{c_b} \pm \sqrt{ -\frac{1}{45} \left(\frac{c_s}{c_b} \right)^2 + \frac{2}{45} \frac{c_s}{c_b} \frac{\Delta B}{b} \frac{b}{h} \left(\left(\frac{\Delta B}{L} \right)^2 + 1 \right) }}{4 \left[\frac{1}{45} \frac{\Delta B}{b} \frac{b}{h} \left(\left(\frac{\Delta B}{L} \right)^2 + 1 \right) - \frac{1}{15} \frac{c_s}{c_b} \right]} \tag{170}$$

B.1.7 Power of the shear force

$$\tilde{P} = \frac{P}{c_b u_0^3 h L} \tag{171}$$

$$= \frac{c_s}{c_b} \int_0^1 \left(1 - \frac{u_\omega \left(\beta, b/2 \right)}{V_0} \frac{V_0}{u_0} \right)^3 d\beta \tag{172}$$

$$= \frac{c_s}{c_b} \int_0^1 \left(1 - 4 \frac{V_0}{u_0} \left(1 - \beta \right) \beta \right)^3 d\beta \tag{173}$$

$$= \frac{c_s}{c_b} \int_0^1 \left(1 - 4 \frac{V_0}{u_0} \beta + 4 \frac{V_0}{u_0} \beta^2 \right)^3 d\beta \tag{174}$$

$$= \frac{c_s}{c_b} \left[-\frac{16}{35} \left(\frac{V_0}{u_0} \right)^3 + \frac{8}{5} \left(\frac{V_0}{u_0} \right)^2 - 2 \left(\frac{V_0}{u_0} \right) + 1 \right] \tag{175}$$

B.2 Mathematical model N°2

B.2.1 Relation between V_0 and $\tilde{V}_0$

$$\int_{\frac{b}{2}}^{\frac{b+\Delta B}{2}} u_1(y)dy = \int_{\frac{L}{2}}^{L} v_2(x)dx \tag{176}$$

$$\int_{\frac{b}{2}}^{\frac{b+\Delta B}{2}} -V_0\frac{2}{\Delta B}\left(y - \frac{b+\Delta B}{2}\right)dy = \int_{\frac{L}{2}}^{L} \tilde{V}_0\left(x - \frac{L}{2}\right)\frac{2}{L}dx \tag{177}$$

The development is the same as the one for the first model, see Appendix B.1.3. So, the final result is :

$$\boxed{\tilde{V}_0 = \frac{\Delta B}{L}V_0} \tag{178}$$

B.2.2 Momentum balance equation in the recirculation
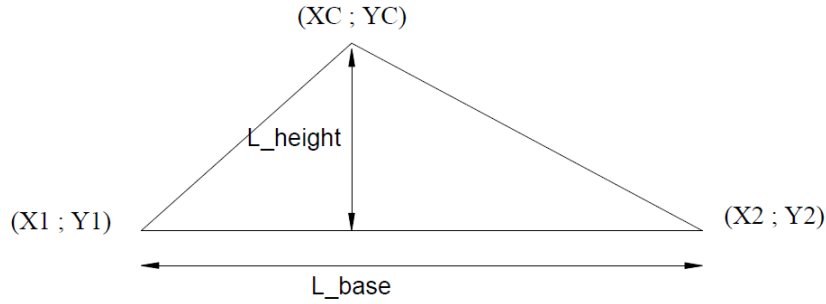
Method of triangles

FIGURE 61 – Sketch and notations of reference triangle

$$X_B = \frac{(X_2 - X_1)^2 X_C + (Y_2 - Y_1)^2 X_1 - (Y_1 - Y_C)(X_2 - X_1)(Y_2 - Y_1)}{(X_2 - X_1)^2 + (Y_2 - Y_1)^2} \tag{179}$$

$$Y_B = \frac{(Y_2 - Y_1)^2 Y_C + (X_2 - X_1)^2 Y_1 - (X_1 - X_C)(X_2 - X_1)(Y_2 - Y_1)}{(X_2 - X_1)^2 + (Y_2 - Y_1)^2} \tag{180}$$

$$L_{base} = \sqrt{(Y_2 - Y_1)^2 + (X_2 - X_1)^2} \tag{181}$$

$$L_{height} = \sqrt{(Y_B - Y_C)^2 + (X_B - X_C)^2} \tag{182}$$

For a linear distribution, the integrale of the square velocity on the surface writes :

$$\int\int_S v^2 dS = V_0^2 L_b L_h \int_0^{L_h} \left(\frac{s}{L_h}\right)^3 ds \tag{183}$$

$$= V_0^2 L_b L_h \int_0^1 \xi^3 d\xi \tag{184}$$

$$= \frac{1}{4} V_0^2 L_b L_h \tag{185}$$